Effect of W concentration in the organized Ti-W alloy oxide nanotubes array on the photoelectrocatalytic properties and its application in the removal of endocrine disruptors using real water matrix

Juliana de Almeida[a,c], Verena Mandorino Kaminagakura[a], Marissol Rodrigues Felez[b], Carlos Ponce de Léon[d], Rodnei Bertazzoli[e], Christiane de Arruda Rodrigues*[a,c]

[a]Department of Chemical Engineering, [b]Department of Chemistry, Instituto de Ciências Ambientais, Químicas Farmacêuticas, Universidade Federal de São Paulo, Rua São Nicolau, 210, Diadema, SP, 09913-030, Brazil.

[c]Unesp, National Institute for Alternative Technologies of Detection, Toxicological Evaluation and Removal of Micropollutants and Radioactives (INCT-DATREM), Institute of Chemistry, P.O. Box 355, 14800-900 Araraquara, SP, Brazil.

[d]Electrochemical Engineering Laboratory, Department of Mechanical Engineering, Faculty of Engineering and Physical Sciences, University of Southampton, University Road Southampton, SO17 1BJ, United Kingdom.

[e]School of Mechanical Engineering, Universidade Estadual de Campinas, Rua Mendeleyev, 200, Campinas, SP 13083-860, Brazil.

***Corresponding author**

Name: Christiane de Arruda Rodrigues

Phone:+55 11 3385-4137 (extension 3538)

Address: Laboratório de Engenharia e Controle Ambiental, Departamento de Engenharia Química, Universidade Federal de São Paulo, São Nicolau St., 210, Diadema, São Paulo State, Brazil, 09913-030.

E-mail address: christiane.arruda@unifesp.br (C. A. RODRIGUES)

Abstract

To evaluate the tungsten content on the photoelectrocatalytic properties of self-organized nanotubes grown by anodization on Ti-xW (wt%) alloys, where x is 0.5, 2.5 or 5.0, this work investigated the phase transformation of TiO_2, the tungsten oxidation states in the oxide layers and their photoelectrocatalytic performance in the degradation of estrone (E1) and 17α-ethinylestradiol (EE2). These films were employed in photocatalytic and photoeletrocatalytic removals of hormones from synthetic and real water matrices. In synthetic water, E1 and EE2 removals, reached efficiencies of 92% and 71%, respectively, after 2 min under UV-Vis photoeletrocatalysis using NT/Ti-5.0W as catalyst. About 30 times longer was needed to degrade 77% of both hormones from the real water matrix due to the presence of other high organic charge. The high performance of the NT/Ti-5.0W was associated with the combination of doping (W-

doped TiO_2) and WO_3 (W^{6+}) heterojunction. However, this electrode had its stability compromised under long degradation times, mainly under visible light, due to a WO_3 leaching process. As for NT/Ti-0.5W, the substitutional W-doped TiO_2 contributed to its greater stability and efficiency for a long time. The low performance of NT/Ti-2.5W was justified by high density of oxygen vacancy and unfavorable position of its adsorption bands.

Keywords: hormones; nanotubes; photoelectrocatalytic degradation; real water matrix; Ti-W alloy; tungsten oxide.

Introduction

Emerging contaminants (or so-called micropollutants) have gained prominence in the last decades due to ecotoxicological risks for ecosystems and living beings at low concentration (μg L^{-1} and ng L^{-1}). Among these micropollutants, the endocrine disrupting compounds (EDCs) have attracted the attention of environmental and health authorities due to the capacity to alter organisms' endocrine functions, promoting adverse effects on human health under chronic exposure [1,2]. Most of endocrine effects are caused by the estrogenic hormone, since they are biologically active and responsible for various types of cancers [1,3], feminization of male fish and reptiles, hermaphroditism, and hormonal dysfunction in human and aquatic beings [4–6].

Estrogens are introduced in the environment by the excretion of not metabolized fraction by living beings to sewage treatment unities; by inappropriate disposal of expired or unused medicines; and by the use of fertilizers from the excretion of medicated animals [3,7]. In general, estrogenic hormones present low water solubility and high affinity for lipids. However, when excreted by mammals, they are conjugated with acids or sulfates which makes them up to 50 times more soluble in water [8,9].

Hormones may be natural, such as estrone (E1) and 17β-estradiol (E2), or synthetic, such as 17α-ethinylestradiol (EE2) [1]. Hormone concentrations in raw and treated sewage can vary according to the consumption pattern of each region and the type of treatment used. According to works reported by Montagner (2017) [10], concentrations of up to ~ 3180 ng L^{-1} and 176 - 2080 ng L^{-1}have been determined in domestic sewage, raw and treated, in Brazil, respectively, for the hormones EE2 and estrone. In surface and untreated supply waters, the scenario is not different either, reaching maximum concentrations of up to 5900 ng L^{-1} and 1800 ng L^{-1} for EE2 and E1, respectively [10]. This is because in Brazil the most of sewage and drinking water treatment plants are predominantly based on conventional treatments. The sewage treatment steps involve elimination of coarse solids, adsorption, sedimentation, or coagulation, aerobic or anaerobic biodegradation, hydrolysis or nitrification, and disinfection, while the water treatment plants are composed by unitary operations of solid-liquid separation, such as coagulation, flocculation,

sedimentation, filtration and disinfection by chlorination. Although these plants are efficient for nutrient removal and microbiological decontamination, they do not remove the estrogen [11,12].

Techniques such as membrane filtration[13,14], ultraviolet radiation[15], ozonization [16] and activated carbon adsorption [17] can, within their limitations, promote a high rate of removal of emerging pollutants when associated to the conventional treatments [12,18]. However, some of these alternatives require a high operating cost, generating an additional cost which is not always absorbed in the drinking water distribution market. While others only concentrate the pollutant load, transferring the pollutant to landfills or other media, or are responsible for converting the pollutant into other substances, sometimes with greater toxicity.

A promising technology that has been enabling the expressive reduction of these contaminants is the heterogeneous photocatalysis, because it allows, depending on the composition and morphology of photocatalyst, the utilization of the visible light from solar energy and the association with a bias potential, which is called photoelectrocatalysis. Then the choice of the photocatalyst is a key component in this process.

Among the different types of photocatalysts explored, the self-arranged TiO_2 nanotube structures have attracted wide attention due to the benefits in their electronic and photocatalytic properties compared to that of the nanoparticles and randomly-oriented particulate TiO_2, such as high electron mobility, high mechanical strength and surface active sites and low quantum confinement effects [19–22]. These nanostructures also present large specific surface area and surface to volume ratio, and the single characteristics of TiO_2, such as non-toxicity, corrosion stability and low cost [22]. However, as well as the other morphologies of TiO_2, its application in water treatment is limited due to the rapid electron-holes recombination rate and its large band gap energy (~3.2 eV). In order to overcome these deficiencies, many researchers have modified self-organized TiO_2 nanotubes by noble metal, metal oxide or no metals but using decoration or doping processes [21,23–26]. While the doping process is often used for narrowing the optical band-gap and to enable a visible light photoresponse by introducing intermediate state(s) in the band gap and/or narrowing the gap itself, the decoration technique promotes hetero-junction formation that changes the surface band bending, reducing the electron-hole recombination, and the suitable surface states creation that improve the charge transfer.

In general, tungsten trioxide is a promising semiconductor to combine with TiO_2 due to small band gap (2.3 – 2.8 eV), which is advantageous for absorption of visible light, and the position of valence band (2.7 eV) and conduction band (0.25 eV), which are lower for WO_3 than for TiO_2. As a result, the charge transfer between the oxide bands is permitted and the charge carrier recombination is inhibited [27–30]. Various studies were reported to enhance the photocatalytic activity of TiO_2 by doping or decorating with WO_x [27,31–34]. However, the photocatalyst preparation procedure, the crystalline structure and the amount of W species in the oxide play a crucial role in the photocatalytic performance of the system.

WO_3 doped self-organized TiO_2 nanotubes using different techniques, such as Ti anodization in electrolyte containing different concentration of WO_{4-2}[34], Ti-W alloy anodization [31,32] and WO_3 loaded TiO_2 nanotubes upon self-doping process [33], showed that the incorporation of small and optimized WO_3 quantities into TiO_2 nanotubes, around 0.21 at% (1.06 wt%) is required to improve the photocatalytic performance of the TiO_2 nanotubes. Additionally, the introduction of the defects and oxygen vacancies in the lattice of WO_3 and TiO_2, by the presence of W^{5+} and Ti^{3+}, contribute to reduce the charge transport resistance and charge carrier recombination, improving its photocatalytic efficiency compared than that of the TiO_2 nanotubes [35]. The incorporation of oxygen vacancies also decreases the interfacial resistance that exists across the electrode and electrolyte interface [36,37]. But the excessive oxygen vacancies in the bulk can act as a recombination center of electrons and holes photogenerated [33]. On the other hand, the TiO_2 nanotubes decorated with WO_3 electrodeposited exhibited the best photocatalytic performance with amount of 1.27 at. % W, as a consequence of the improvement of the electron / hole separation, thereby increasing the half-life of holes directed towards the electrode surface. But for W content more than 2 at %, the photocatalytic activity of TiO_2-WO_3 composite reduced drastically, because some of the WO_3 sites acted as charge recombination centers [27].

Under visible light, the photocatalyst performance of oxide nanotubular structures grown on Ti-9W (at.%) (i.e. W content very upper limit of WO_3 doping) was similar than that for TiO_2 nanotubes [31]. However, under anodic potential current multiplication reactions occur, that are favored by WO_3 in the oxide layer [31]. The literature also suggests that the presence of WO_3 in TiO_2 influence to the formation of activating surface species such as W^{6+} states that acts as mediators for charge transfer to the electrolyte [31,32]. The water oxidation and organic molecule degradation are favored on (002) facet on monoclinic WO_3 via consuming photo-excited holes and generation active oxygen species, contributing to reduce the recombination of photogenerated carriers. The monoclinic crystalline phase is the most stable at room temperature and it is obtained by the transformation of $WO_3.H_2O$ from orthorhombic into hexagonal structure and finally to monoclinic phase during the heat treatment of WO_3 composite [38]. Normally the temperature conversion occurs from 400 to 500 °C, but in oxide nanotube arrays this transformation is strongly dependent of the composition of the oxide and of the substrate on which it has grown [39,40].

Despite the good performance of self-organized TiO_2 nanotubes modified with WO_3, there are few studies on their application in the area of water and effluent treatments. Most applications are concentrated in electrochromic devices [41], water splitting [42] and hydrogen storage [43].

Then, motivated by the previous results of hormones degradation using oxide nanotube arrays grown on Ti-0.5W (wt.%) [44], associated to the highest level of this micropollutants in water stream of Billings Reservoir from Brazil [45], and the lack of information about the role of W concentration in doping or heterojunction formation, this work investigated the characteristics and photoelectrocatalytic performance of oxide nanotubular layer grown on Ti-xW (wt.%). For

ethinylestradiol (EE2) and estrone (E1) degradation experiments, the selected values for x were 0.5 (0.13 at.%), 2.5 (0.65 at.%) or 5.0 (1.35 at.%). Characterization studies of the photocatalysts were carried out in order to elucidate the effect of the W content in relation to the type of the substrate microstructures, the phase transformation of TiO_2 nanotubes and the tungsten oxidation sates in the oxide layers. The photo-electrocatalytic performance of these electrodes was evaluated under UV and visible light, in a synthetic and real water matrix from Billings Reservoir, an important water supply source for the Metropolitan region of São Paulo in Brazil. The substrate microstructure interferes in the resulting tungsten state of oxidation (W^{4+}, W^{5+} or W^{6+}) obtained by the anodizing process. Tungsten oxidation states and concentration result in different TiO_2 modification processes as doping and/or heterojunction formation. Thus, the amount of W in the alloy was chosen to evaluate the contribution of the unique doping phenomena and the combination of the doping and heterojunction process on the photocatalytic activity of semiconductors. For this, the limit of solubility of W in the Ti-W alloy, around 0.73 wt% (0.2at.%), was taken into account [46], since the W amount below this limit can favor the doping process in the substrate.

1. Materials and Methods

1.1. Electrode preparation and characterization

Ti-xW(wt.%) alloys (x = 0.5, 2.5 and 5.0) were prepared by arc melting under argon atmosphere, using 99.95% titanium (Ti-Brasil) and 99.9% tungsten powder (Aldrich, 12 μm). These ingots were remelted three times to assure the homogeneity of its chemical composition and subsequently cooled inside the furnace under the inert atmosphere to avoid oxidation of the alloy. After melting and solidification, the alloy bars were submitted to a hot rolling process and cut in foils shape of 30 mm in length × 50 mm in width × 2 mm thick. For obtaining micrographs, the substrates were polished and etched using Kroll's solution (HNO_3 and HF in H_2O) and characterized using an optical microscope ZEISS Axiolab 5 connected with a Cam ZEISS AxioCamERc 5s. The elemental composition of these alloys was verified with an X-ray fluorescence Spectrometer (XRF – BRUKER Tiger) and phases composition of the substrates were identified by Rietveld refinement method from XRD analysis.

Then, the substrates were placed as working electrode in an electrochemical cell and a Pt plate as the counter electrode to obtain nanotube layers by anodization process. The samples were anodized in ethylene glycol (MERCK) with 0.2 mol L^{-1} HF (48%, MERCK) using a constant potential at 120 V using a power source (Supplier, DC Power Source) coupled to a computer. The time of anodization varied depending on tungsten concentration, being 30 min for Ti-0.5W (wt.%) and 40 min for Ti-2.5W (wt.%) and Ti-5.0W (wt.%) alloys. Self-organized TiO_2nanotubular array

(NT/TiO_2) used for comparing with self-organized nanotubular oxide layer grown on Ti-xW (wt.%) (NT/Ti-xW) was anodized under potential of 20 V during 6 h in ethylene glycol. During these experiments, an Autolab PGSTAT302 potentiostat / galvanostat coupled to an ET 2042 C voltage multiplier was used as supply source.

After anodization, the samples were rinsed with deionized water and dried under a N_2 stream. The structural characterization of the anodized layers was performed with a field emission scanning electron microscope (SEM-FEG, FEI Inspect F50). Cross-sectional images of the layers were obtained from mechanically scratched samples.

Nanotubular array layers grown on Ti sheet was annealed at 450°C; while that obtained on Ti-0.5W (wt.%), Ti-2.5W (wt.%) and Ti-5.0W (wt.%) alloys were heat-treated at different temperatures from 350 to 650 °C for 150 min in atmospheric air in a muffle furnace (EDG, F3000). XRD data were collected at room temperature on a Bruker Advance D8 diffractometer equipped with Cu Kαradiation, a Bragg−Brentano optical module and a position-sensitive Lynxeyes detector. The angular range covered was 2θ =20−90° and a step size of Δ2θ = 0.020° was used. Rietveld refinement of XRD patterns was carried out using DIFFRAC.TOPAS software package. The photoelectrochemical measurements were performed in a single compartment electrochemical cell configured in a conventional mode of a three-electrode with Pt foil as the counter electrode and silver/silver chloride (Ag/AgCl) in 3 M KCl as the reference electrode, conducted with an Autolab PGSTAT302. The electrolyte solution employed was 0.5 mol L^{-1} HCOONa (sodium formate) for cyclic photocurrent and chopped light voltammetry was carried out in 0.2 mol L^{-1} Na_2SO_4, pH 2.0. In both experiments, the exposed area of the working electrode was 0.282 cm^2under UV/Vis irradiation equivalent 1 sun (100 W/cm^2) emitted by an 80 W Hg lamp.

Photoelectrochemical electrode stability tests employed chronoamperometric measurements at a fixed potential of 1.5 V *vs*. Ag /AgCl using real water matrix during 1 h for E1 and EE2 under UV-Vis and using visible light the time was monitored during 1h for E1 and 8h for EE2.

Raman spectra were obtained on a Renishaw in Via model, with He-Ne excitation laser. Absorbance data were performed from UV-Vis-NIR diffuse reflectance with a Shimadzu UV-2600 spectrophotometer, equipped with an Integrating Sphere. The equipment was calibrated with barium sulphate standard (Labsphere USRS-99-020) and the spectra range was recorded from 250 to 800 nm. The PL spectra were measured using a Thermal Jarrel-Ash Monospec 27 monochromator and Hamamatsu R955 photomultiplier with a krypton ion laser (Coherent Innova 200 K) as the excitation source. The photoluminescence spectrum covered electromagnetic signals in the visible range between 320 and 750 nm and the line of excitation was kept at 350.7 nm. X-ray photoelectron spectroscopy (XPS) was performed at high-resolution (HR) using a K-alpha spectrometer (Thermo Scientific) coupled with monochromatic Al Kα radiation (E = 1486.6 eV) and a hemispherical electron energy analyzer. The energy bandpass applied was 0.05 eV and

the spectra were deconvoluted by linear background subtraction and then fitted with Gaussian functions.

1.2. *Degradation experiments*

Photolytic, photocatalytic and photoelectrocatalytic degradation experiments of E1 and EE2 were carried out in a glass electrochemical cell with a single compartment and cooling jacket. The NT/TiO_2 or NT/Ti-xW photoanode and a platinum grid cathode were placed in parallel inside of the reactor in a 40 mL of working solution consisting of deionized / natural matrix water with added E1 or EE2 (10 mg L^{-1}) at pH 6 and 4, respectively. All electrodes were connected to a power supply (Advancy Simple Power Supply, ADV-3052V) and bias potential applied on the photo-anodes was 1.5 V. A Hg lamp (80 W) enclosed in a tubular quartz sleeve placed outside the reactor was employed as light radiation source equipped with IR filter. The incident light was adjusted at 100 mW·cm^{-2} at the surface of the photoelectrode using a calibrated UV light meter. For visible light illumination, a purple LED (50 W) with emission at 405 nm was used as source. All the experiments were performed at room temperature (~ 25 °C). During the treatment 0.5 mL aliquots were removed using a syringe at regular time intervals.

The deepwater from Billings Reservoir, an important drinking water source for the Metropolitan region of São Paulo in Brazil, was investigated as a real matrix in this study. Real water matrix samples were collected in column water at 5 m of depth in triplicated using Van Dorn bottle in (latitude: 23°43'17.5"S, longitude: 46°38'00.6"W) point and stored in 1 L capacity sterile plastic bottles. All samples were refrigerated during transportation to the laboratory for degradation experiments. The water parameters were obtained from the previous studies [47], such as temperature (23 °C), pH 6.9, electric conductive (213 μS cm^{-1}), dissolved oxygen (9.05 mg L^{-1}), total particulate (173,1 μg L^{-1}), chlorophyll (9.3 mg L^{-1}) NO_2 (162,3 μg L^{-1}) NH_4 (609, 8 μg L^{-1}) NO_3 (2540 μg L^{-1}), and total nitrogen (1769,4 μg L^{-1}). The presence of hormones (EE2 and E1) was not observed in real water matrix, probably the concentrations of these estrones were below the lower limit detection (LOD) of the HPLC technique, as values reported by [44]. In addition, the total organic carbon of real water matrix showed 557 ppm (Table S1) and also, UV-Vis spectra showed organic compounds in the composition (**Figure S8**).

In order to ensure the adsorption-desorption equilibrium, the concentration changes of the pollutant in real water matrix by were monitored by measuring the peak of chromatographic spectrum after contact of NT/Ti-xW during11 min in the dark. The aliquots of 750 μm were taken out at regular intervals time.

1.3. Analytical Methods

High performance liquid chromatography (HPLC) using a laser-induced fluorescence detector (LIF) was the technique chosen to separate and evaluated the estrone (E1) and17-α-ethinylestradiol (EE2) standards and their by-products. The HPLC method was developed and validated according to demonstrated by Oliveira and co-authors (2020) [44].

2. Results and Discussions

3.1 Preparation and Characterization of self-organized nanotubular oxide layer on Ti-W alloys

The results of XRF analysis from the Ti-W alloys are shown in **Table 1**. The chemical composition of the samples was close to the nominal compositions, indicating that the casting procedures were appropriate. As the W amount in the Ti-0.5W (wt%) alloy is close of the detection limit of XRF equipment, its composition was also confirmed by ICP-MS analysis.

The optical micrographs obtained from samples of the Ti-0.5W (wt. %), Ti-2.5W (wt. %) and Ti-5.0W (wt. %) (**Fig. S1**) exhibited a lenticular region separated by darker fields. The lenticular region may be associated with the primary Ti-α (white phase), while the dark phase was related to Ti-β and W precipitated, as observed on the Ti-W system diagram [46]. On the Ti-0.5W (**Fig. S1a**), the lamellar microstructures can be associated with the doped Ti-α phase (solid solution) [48], as identified by the Rietveld method (**Table 1**). The Ti-α phase is an equilibrium phase at lower temperatures and its formation is associated with the slow cooling. Furthermore, the solid solution formation is favored when the tungsten content is below the solubility limit in the Ti-W system (e.i. ≤ 0.73wt%W) [46] and, as a consequence the substitutional chemical doping that occurs due to the insertion of W on the Ti crystal lattice. For the other samples, which W content is higher, the presence of Ti-β phase was detected by Rietveld methods (**Table 1**) and it can be present together with W precipitated in dark regions of optical microscopy in **Fig. S1b** and **c**.Ti-β corresponds to metastable compound at room temperature, which can be decomposed when subjected to an aging treatment in the field. For metastable phase of Ti-W system, the solubility of W increases and reaches a ratio of 1:1 in the crystal lattice of the Ti-β [48]. However, due to size incompatibility between the atomic radii of these elements, W is easily removed from the lattice in the solid phase, leading to the positioning of W between the interstices of the Ti crystal lattice.

Rietveld refinement method from the diffractograms of Ti-W alloys (**Figure S2a**) showed that the quantity of Ti-β phase and W precipitate increased as W elemental concentration. For Ti-0.5W substrate, only Ti-α and doped Ti-α phases were identified, while for, Ti-5.0W and Ti-2.5W alloys higher quantity of Ti-β is present but in more quantity for Ti-5.0W. This observation is in agreement with its close position to the eutectoid reaction, as indicated on the Ti-W phase diagram

[48]. The sum of atomic percentages obtained for Ti-α, Ti-β and W content for all samples corroborated with the results from ICP-MS and XRF analysis. As mentioned above, the Ti-α is predominant in all samples and the W content in the substrate can be present by chemical doping and/or precipitation. This evidence is based on shifting the position of the Ti-α peaks towards the higher 2Θ values as consequence to expansion of the Ti crystal lattice, as observed in **Figure S2b.** This expansion occurs because ionic atomic radius of tungsten (193 pm) is slightly smaller than that of titanium (176 pm) [49]. The greater the amount of tungsten, the greater the displacement of peaks in the X-ray diffraction spectrum, due to a greater incorporation of W inside the crystalline lattice.

In a previous work, Tsuchiya and co-authors [50] observed that the variation in the chemical composition of the alloys and/or the anodic oxidation parameters had a stronger effect on the nanotube layer features. In an organic solution, the anodization time has a crucial influence on the tube length [51]. In order to obtain a self-organized nanotubular oxide layer with comparable dimensions (length and inner diameter), the anodization conditions for Ti-xW (wt%) alloys (x = 0.5, 2.5 and 5.0) were optimized in relation to the anodization time under constant applied potential of 120 V, as shown in **Figure 1**. For all samples, the increase in anodizing time resulted in an increase in the length of the nanotubes until reaching a maximum length. After this time, the thickness of the oxide layer decreases due to an increase in dissolution of the nanotubular oxides and the formation of nanograss [44]. Similar behavior was observed for the inner diameters of the tubes. To produce nanotubes with a tube length around 6 μm (obtained from SEM cross section) and an inner diameter between from 40 nm to 75 nm (obtained from SEM top image) were applied 120 V during 30 min for Ti-0.5W (wt%) substrate and 40 min for Ti-2.5W (wt%) and Ti-5.0W (wt%) alloys (**Figure 1a**).

The difference in the anodization time can be associated with the phase features in a substrate's microstructure. For the Ti-0.5W (wt.%) alloy, the Ti-α phase is predominant in this substrate and tungsten is present in solid solution (doped Ti-α). For other alloys, part of W is also present in Ti- β phase and the excess of tungsten forms a small volume fraction of W precipitated in Ti-α [46]. **Figure 1.b-d** shows the top view and the cross section of oxide layers grown on Ti-W alloys. For future comparison, pure Ti sample was also anodized at 20V for 6 h, under conditions mentioned in previous work [44].

The self-organized nanotubes produced by anodization process are amorphous, so they need to be submitted a thermal treatment to convert them in a crystalline structure. To study the effects of the temperature in the anatase and rutile transformation, XRD analysis were carried out for all samples and the results shown in **Figure S3**. The anatase (A) and rutile (R) phases were detected in diffraction angles (2Θ) of 25.28 (JCPDS, Card No. 21-1272) and 27.44(JCPDS, Card No. 21-1276), respectively, that represent the mainly crystal plane of these phases. At 450 °C, a small intensity peak of rutile was detected for samples with higher W amount in comparison to pure Ti

and Ti-0.5W (wt%) samples (**Figure S3**). This indicates that the tungsten can delay the phase transition (from anatase to rutile). To elucidate this effect, the volume fraction of anatase and rutile during this transformation was calculated by using the diffraction peak intensities for each phase and by applying the equations suggested by Slimen and co-authors [52]:

$$f_A = \frac{K_A \cdot I_A}{[K_A \cdot I_A \cdot I_R]} \quad (1)$$

$$f_R = \frac{I_R}{[K_A \cdot I_A \cdot I_R]} \quad (2)$$

where f_A and f_R correspond the volume fractions of the anatase and rutile phases, respectively, K_A is a constant of 0,886, and I_A and I_R refer to the intensity of diffraction peak from anatase (101) and rutile (110), respectively. **Figure 2a** shows the anatase (black color) and rutile (red color) volume fractions as a function of the heat treatment temperature of the oxide layer grown on pure Ti and Ti-W alloys. In all plots the sum of the volume fractions of anatase and rutile phases will be 100 %. At 350 °C, the crystallization of oxide layers is not completed, because no evidence of rutile phase is observed in all samples. But at temperature above 400 °C an amount of rutile has been formed on the nanotube walls for NT/Ti-0.5W and NT/TiO_2, while for NT/Ti-2.5W and NT/Ti-5.0W this formation was detected only above 500 °C, as shown in **Figure 2a**.

The evolution of the volume fractions of anatase and rutile formed on NT/TiO_2 and NT/Ti-0.5W (Fig. 2a) shows that a mixture of 50 % anatase and 50 % rutile occurred at around 600 °C and at ~ 575 °C, respectively. During the anodization process, the W species diffuse into the TiO_2 crystal lattice and replaces the Ti^{4+} atoms. Consequently, the density of the oxygen vacancies is increased, resulting in greater mobility of atoms and acceleration of the phase transformation compared to NT/TiO_2. However, when the W amount introduced in TiO_2 crystal lattice exceed of solubility limit in the oxide layer, the interstices are occupied, resulting in retardation of the phase transformation, as observed for NT/Ti-2.5W and NT/Ti-5.0W. For these samples, the equal mixture of anatase and rutile was not reached up to 600°C. But it is noticed that the phase transition is slower for samples with high content of W.

To find the best temperature, in which anatase to rutile ratio promotes high photocatalytic performance, photocurrents experiments were carried out and the results are shown in **Figure 2b-d**. For NT/$TiO_2$and NT/Ti-0.5W, high current values were obtained at 450°C, while for NT/Ti-2.5W and NT/Ti-5.0W the best heat treatment temperature was 550 °C, probably due to the presence of the rutile in the oxide, in agreement with the results of **Figure 2a**. According to the phase diagram [48], the phase transitions of the Ti-W alloy occur between 882 and 740 °C for all alloys. So, the crystallization temperatures of the oxide layer grown on the alloys (450 and 550 °C) will not promote phase transformations of the substrate.

Figure 3 shows the XRD patterns of all the samples after heat treatment under the optimized temperature determined in the photocurrent experiments. For all the samples, the diffraction peak of anatase phase (2Θ = 25.28) appears with more intensity than that of rutile phase (2Θ = 27.48). For NT/TiO_2 modified with tungsten, a slight shifting of these peaks towards the higher 2Θ values in relation to NT/TiO_2 is observed, indicating a contraction in the TiO_2 unit cell (**Figure 3a**). In addition, the Ti-α phase (2Θ = 40.19) appears in all diffractograms. No tungsten oxide phase could be observed in NT/Ti-0.5W sample because it is highly dispersed in the TiO_2 crystal lattice and the concentration of tungsten oxide is too low of detection limit for XRD analysis, as reported by Oliveira and co-authors [44]. In contrast, reflections correspondent to tungsten oxide species are seen for NT/Ti-2.5W and NT/Ti-5.0W. When the W amount exceeds over that required for doping process, crystalline WO_{3-x} ($0 \leq X \leq 2.8$) or/and $Ti_{.54}W_{.46}O_2$ are detected [53–57]. As seen in the **Figure 3b**, the peaks at 2Θ = 70.48° and 2Θ = 72.03° corresponds to WO_{3-x} and that at 2Θ = 70.71° corresponds to $Ti_{.54}W_{.46}O_2$, in agreement with the studies made by SAJJAD and co-authors [58]. In general, WO_{3-x} ($0 \leq X \leq 2.8$) refers to the shifting position of tungsten oxide peaks (stoichiometric or non-stoichiometric) due to the presence of oxygen vacancies. The absence of oxygen leads to structural relaxation around the vacancy, causing an increase in the distance between the W-W atoms and therefore, inducing changes in the 2θ values to the species O-W-O [53,59,60].

As mentioned above, the composition of the nanotubular matrix can be influenced by the phases present in the substrate due to the mechanism for obtaining them through the anodizing process [61]. The phases of the Ti-W alloy during growth show different kinetic rates of chemical dissolution and interact differently with the electrolyte [19]. As a result, small changes in morphology can occur as noted by Luz et. al. [61] and the formation of nanostructures with different oxidative species and arranged in different ways may be observed under biphasic alloys, as observed in X-ray diffraction that showed a mixture of tungsten oxides. The solid solution (W substitutional doping Ti-α) during the anodic process can more easily lead to the formation of oxides ternary, due to the already existing bond between Ti and W atoms inside the crystal lattice. Meanwhile, the Ti-β phase, after its dissociation leads to the presence of W between the Ti interstices, favors the formation of non-stoichiometric tungsten oxides (WO_{3-x}) and therefore, high density of oxygen vacancies. The inner position of the interstitial W affects the limitation of reaction with oxygen present at the oxide / electrolyte interface during the formation of Ti-W nanotubes by anodization process, leading to the formation of oxides rich in defects by forcing oxygen sharing between Ti species and W. The W precipitate, from excess non-dissolved on Ti-α e Ti-β phases, shows greater contact with the electrolyte during film growth and therefore, the formation of stoichiometric oxide (WO_3) is favored due to non-limitation of oxygen. As a result, it is not linked to Ti and placed in more exposed regions due to deposition of this phase on the edges of the grains during the cooling process.

Figure 4 shows the comparison of Raman profiles for the oxide films grown on Ti-W alloys. The presence of Raman bands at 146, 391, 516 and 636 $cm^{-1}$are typical of the anatase phase and correspond to values close to those reported in the literature [56,58,62,63]. The characteristic peaks of the rutile phase of TiO_2 were not detected in any of the analyzed films, probably due to the low concentration. These results corroborate with the XRD measurements that also showed different amounts between the anatase and rutile phases. The other peaks are associated with the W - O bending modes from the tungsten oxides, which showed very weak absorptions and the absence of typical Raman bands in the region between 800 and 900 cm^{-1}. These results reveal that tungsten oxides are in low concentration, distributed in different stoichiometry in the oxide matrix, and that there are no defects related to the dual W^{+6} = O binding mode.

The comparison of the Raman spectra obtained for NT/Ti-xW films (x = 0.5, 2.5 and 5.0) does not show displacement between the peaks in the different spectra, showing that the oxide layers present stability and little structural distortion even for the annealed films at 550 °C. However, when the peak values for the bonds of Ti and W oxides are compared with those reported in the literature, a displacement of 2 cm^{-1} for all bands is verified, suggesting the formation of vacancies in the structure due to the absence of oxygen and doping of the TiO_2crystal lattice [64]. With the increase of W amount in the oxide layer, the appearance of new bands and/or increase in the intensity of the existing band were noticed. The Raman spectrum of NT/Ti-0.5W sample showed signal only for the W^{5+}–O ionic bond at 326 cm^{-1} [65]. NT/Ti-2.5W sample also presented W^{5+}–O binding and a second band at 447 cm^{-1} attributed to W^{5+}=O interactions [26]. The presence of these bands was also observed in NT/Ti-5.0W film, but with greater intensity and combined with the appearance of hexavalence peaks at 610, 701 and 793 cm^{-1}, referred to the elongation mode of O–W^{6+}–O from WO_3 octahedral unit [65].

In order to investigate the chemical composition and oxidation state of Ti, W and their interactions with O, XPS measurements were performed, and the results are exhibited in **Figure 5**. The peaks from the most energetic level of tungsten (W 4f) are situated between binding energies of 30 and 46 eV. In this region, excitation signals from the Ti 3p layer, intermediate titanium sublevel, are also present and the signal overlap may be occurring. Therefore, both W 4f (**Fig. 5a, 5c and 5e**) and Ti 2p (**Fig. S5**) regions were analyzed to find the composition and/or doping species on the electrode surface. XPS data for NT/Ti-0.5W (**Fig.5a**) showed an intense signal at 38.1 eV and less prominent at 36.2 eV which refer to Ti^{4+} and Ti^{3+}, respectively, in agreement with the values reported in the literature [66]. The other peaks with binding energy at 37.5 and 39.6 eV correspond to W $4f_{7/2}$ and its doublet W $4f_{3/2}$, respectively, which separation of 2.1 eV indicates the presence of W species in the oxide film [67–69]. The average binding energy of 37.5 eV implies that the tungsten dopant is predominantly in the W^{5+} state and does not show undissolved levels such as W^{4+} and W^{6+} [53,70]. The presence of tungsten was also verified in high resolution XPS spectra of the O 1s (**Fig. 5b**). In this region, the peaks centered at 530.6 eV

and 531.0 eV configure the presence of bonds between O-Ti from TiO_2 and from strong interactions between W doping and O atoms, respectively [69]. The insertion of tungsten in the TiO_2 crystal lattice can be verified by comparison to the spectra region of the Ti 2p for NT/TiO_2 and NT/Ti-0.5W films (**Fig. S3b**), where a displacement between the maximum peaks of Ti $2p_{3/2}$ and Ti $2p_{1/2}$ was observed. This displacement is attributed to the electronic disturbance caused by the incorporation of W species in the TiO_2 crystal lattice. This is because the electronegativity of the doping element is slightly higher in relation to Ti, resulting in a decrease in the electron density around the base element and an increase in the binding energy [56,68,71].

For NT/Ti-2.5W and NT/Ti-5.0W samples, whose W concentration is higher, the deconvolution of W4f and Ti2p peaks indicated the presence of W^{4+}, W^{5+} and W^{6+}, evidenced by the displacement of 1.5 eV between the spin-orbit peaks and their doublets, as shown in **Fig. 5c** and **5e**. Based in the literature, the W^{6+} and W^{5+} are originated from WO_{3-x} ($0 \leq x \leq 0.28$) species [53,72–74] and the $W^{4+}$is from the non-stoichiometric ternary oxide $Ti_{0.54}W_{0.46}O_2$ [57]. According to Eibl and co-authors [75], the valence of tungsten in the ternary oxide composition is directly related to Ti, and may assume W^{4+}, W^{5+} or W^{6+} when linked to Ti^{4+}, Ti^{3+} or Ti^{2+}, respectively [57]. However, the W^{4+} is more favorable to react with Ti^{4+} in the crystalline cell, favoring the synthesis of ternary oxides through the coalescence of species from the Ti-O-W system provided by the solid solution [57,75].

The main difference between NT/Ti-2.5W and NT/Ti-5.0W samples consists of the variation in the intensities of W^{5+} and W^{6+} and the existence of a weak peak reported at 44.6 eV for only the NT/Ti-2.5W sample. This peak is attributed to the binding energy of W $5p_{3/2}$ and its presence is associated with a greater amount of W^{5+} in relation to the W^{6+} and consequently with the number of defects. On the other hand, the oxygen vacancies in the Ti matrix, resulting from changes in the electronic density of the material caused by the increase in temperature, may be associated with the valence W^{5+} [76,77]. However, the difference in the intensities of W^{5+} and $W^{6+}$for NT/Ti-2.5W and NT/Ti-5.0W samples can also be influenced from the phases of the substrate used to obtain the film. Although both substrates have the Ti-α solid solution as the majority equilibrium phase in the composition, the Ti-2.5W alloy presents a smaller portion of the W precipitate compared to the Ti-5.0W alloy [46]. Therefore, it can be concluded that the phases that make up the metallic substrate act as precursors in the formation of the oxide film, influencing its composition and in the amount of W^{5+} and W^{6+}present in NT/Ti-2.5W and NT/Ti-5.0W.

The values of peak area ratio for $Ti^{3+}$and Ti^{4+} as well as W^{4+}, $W^{5+}$and W^{6+} are tabulated in **Table 2.** These results showed that the content of W^{4+} and W^{5+} are present in all samples, while the W^{6+} species are present only in those samples which W amount in the substrate is above 0.73 wt.% (0.2 at. %), reaching higher values for NT/Ti-5.0W. Despite the presence of W^{4+} in the oxide layer on the Ti0.5W alloy, which comes from the substitutional W in the Ti crystal lattice, the production of ternary oxide did not occur due to the low amount of W in the oxide layer and the

heat treatment temperature (450 °C). However, in the samples with a higher amount of W and treated at 550°C, the presence of the ternary oxide occurred, as detected in the XRD analyses. For NT/Ti-2.5W and NT/Ti-5.0W samples, the solubility limit of W in the Ti-W alloy was reached, favoring the substitutional (W^{4+}) and interstitial (W^{5+}) chemical doping in the oxide layer, and the precipitation of W excess that is responsible for WO_3formation (W^{6+}). About the presence of oxygen vacancies, it can be observed from **Table 2**that it is greater in the NT/Ti-2.5W sample compared with the other samples due to its highest amount of W^{5+} species.

Figure 5d-f indicates the O1s spectra for NT/Ti-2.5W and NT/Ti-5.0W samples. Both spectra showed similarity in the composition, showing peaks centered at 530.8 eV (WO_{3-x}), 532.4 eV (O-W^{4+}), 530.5 eV (O-Ti^{4+}), 531.3 eV (O-Ti^{3+}) and 532.5 eV (OH^-).While the O-W bonds are associated with the O_2^- vacancies, the O-H^- bonds can be a confirmation of the presence of defects due to the imminent adsorption of H_2O vapors on the electrode surface [29]. These groups help maintain charge balance in oxygen deficient regions through bonds with metal cations. Then, the presence of the OH^- group on the surface of the nanotubular oxide layer may be related to the oxygen vacancy density [78].

Based on the characterization results of oxide layer of all samples, we concluded that the doping process is presented in all oxide layers modified with W content, evidenced by the displacement in XRD patterns and XPS spectra of NT/Ti-xW (x = 0.5, 2.5 and 5.0) compared with that of NT/TiO_2. For NT/Ti-0.5W, the substitutional doping process was partial because the W amount was below of solubility limit of W in the Ti crystal lattice. For other samples which the limit of solubility of W in the Ti-W alloy is higher than 0.73 wt% (0.2at.%), the substitutional and interstitial chemical doping took place. Precipitation of W also occurred in the samples with higher content of W, mainly in the NT/Ti-5.0W, and it was detected by the increase of W^{6+} species in the XPS and Raman analysis.

3.2Photoelectrochemical properties of self-organized nanotubular oxide layer on Ti-W alloys

Figure 6a shows the UV-diffuse reflection spectra of NT/TiO_2 and NT/Ti-xW (x = 0.5, 2.5 and 5.0) samples. All samples exhibit elevated absorption in UV region, except for the NT/Ti-2.5W, where a smaller decrease in the absorption is observed between 250-350 nm. On the other hand, the absorption intensity in the UV light region increased greatly for NT/Ti-5.0W sample, suggesting the presence of WO_3 as observed in XPS spectra (**Figure 5**) and in the literature [79]. With the incorporation of W species in the oxide layer, the shifting of absorption edge towards higher wavelength occurs. The change in cut-off edge is commonly owing to the substitution of Ti^{4+} by W species, increasing the oxygen vacancies and electron concentration.

The presence of a single band after 380 nm for NT/Ti-0.5W indicates the doping of the material. In general, the doping process contributes to increase the oxygen vacancies in the oxide

layer, providing a greater visible light absorption [80]. For NT/Ti-2.5W and NT/Ti-5.0W, the presence of two wide absorption bands between 420 -520 nm and 530-680 nm were displayed. According to the literature [81], these bands are originated from the defects and impurity states generated by ions substitutions in the crystal lattice. In this work the existence of these bands was attributed to the presence of oxygen deficiencies in the oxide, as attested by the formation of sub-stoichiometric WO_{3-x} phases (**Figure 3b**), which it can be responsible for increasing the absorbance in the near-infrared region due to polaron transitions between two non-equivalent sites, W^{5+} and W^{6+} or W^{5+} and W^{4+} [82]. It can also be seen that the intensity of absorption of these bands was higher for the NT/Ti-5.0W sample.

UV-vis DRS measurements suggest that the NT/Ti-5.0W can be considered to have a higher light response than the other two photocatalysts (NT/Ti-0.5W and NT/Ti-2.5W), which is advantageous in photocatalysis processes.

In order to obtain information about the recombination rate of electron/holes pairs in the nanotubular oxide layer before and after incorporation of W species, photoluminescence spectra (PL) of all samples were examined in the wavelength from 350 to 600 nm under excitation of 350 nm, as shown in **Figure 6b**. The spectra consist of a predominantly absorption band located at ca. 440 nm, which is due to the direct transition of electrons from conduction band to valence band [83] The relative emission intensity of this band is maximum for NT/TiO_2 sample, but it recedes with the incorporation of W in the oxide layer. Probably, the photo-generated electrons are transferred from TiO_2 conduction band to the tungsten oxide conduction band and the holes accumulate in the TiO_2 valance band, as suggested by Sajjad and co-authors (2009) [58]. But when the oxygen vacancies amount is higher new recombination centers are created increasing the emission intensity. This phenomenon is observed for NT/Ti-2.5W sample, which emission intensity is similar of NT/Ti-0.5W sample. For NT/Ti-5.0W the result is different due to the presence of W^{6+} in higher amount, creating tungsten oxide conduction band with different energy levels that contribute to reduce the charge recombination.

In the region of 510–550 nm (green emission), there is a weaker absorption band for all samples, which is usually aroused by the intrinsic defects [84]. In commercial ZnO phosphors, the green emission intensity is strongly influenced by free-carrier depletion at the surface oxide, particularly for small particle and/or low doping [84]. For $CaWO_4$ and ZnO nanoparticles, without any doping, the oxygen vacancies appear as the defect responsible and the green emission trends to increase when the particle size is reduced [79,84]. High green emission intensity is observed for NT/Ti-2.5W in **Figure 6b** as consequence of the high oxygen-vacancy density. This result is corroborated with XPS analysis, where the amount of W^{5+} is higher (**Table 2**).

The photoelectrochemical activity of the oxides grown on Ti-W alloys was further investigated under chopped light voltammetry (CLV) by linear sweep voltammetry (LSV), as shown in **Figure 7a**. All linear voltammograms were obtained from scanning the potential from-

0.5 V *vs*. Ag/AgCl towards positive values, passing through the open circuit potentials (OCP) measured at ~ -0.4 *vs*. Ag/AgCl for all combined oxide electrodes. For NT/Ti-xW (x = 0.5, 2.5 e 5.0) samples, the photocurrent density followed a general trend of increase with increasing applied potential, typical behavior of the n-type semiconductor, with an onset potential at ~-0,36 V *vs*. Ag/AgCl. This phenomenon occurs due to higher band-bending at the photo-anode/electrolyte interface, which leads to higher mobility of the photogenerated excitons, and expansion of the depletion width with increasing applied potential [85] until reaching the saturated photocurrent. Similar behavior was observed for NT/TiO_2, but an anticipation of the onset potential for the oxides modified with W occurred compared to the pure electrode. In addition, the maximum current density values for the NT/Ti-0.5W, NT/Ti-2.5W and NT/Ti-5.0W electrodes were 0.78, 0.98 and 1.24 mA cm^{-2}, respectively, which is 1.5, 1.9 and 2.4 times that of NT/TiO_2. The improvement in photocurrent values for tungsten-modified oxide samples can be attributed to the modification in the structure of the electronic bands due to the creation of the tungsten oxide conduction band with different energy levels, which contributed to reduce the charge recombination rate, and to the best use of the light radiation spectrum, as observed from the diffuse reflectance and PL data. Furthermore, the insertion of oxygen vacancies in the TiO_2 matrix may also have effectively contributed to the increase in the photocurrent of the tungsten-modified electrodes.

The photoelectrochemical activity of the electrodes was further investigated by cyclic sweep voltammetry under UV-Vis and visible irradiation, using an aqueous solution containing hole scavenger (sodium formate). The photocurrent densities as a function of applied potential for all samples (NT/TiO_2 and NT/Ti-xW), are shown in **Figure 7b**. For comparison, the dark current densities under no light irradiation were also measured. No change was observed in the dark current densities with an increase in the applied potential for all the samples under UV-Vis and visible irradiation. The maximum photocurrent values obtained for all electrodes are shown in **Table 3**. Compared with the dark current, an increase in the photocurrent is observed for all samples under both irradiations, but under UV-Vis irradiation this increase is significantly higher. Additionally, the highest photocurrent densities occur for oxide layers modified with W species when compared with NT/TiO_2, mainly under visible light, reaching current maximum values 1.5 – 4.7 times higher than that of NT/TiO_2. These results are consistent with the UV-Vis DRS analysis, which shows that NT/Ti-xW (x = 0.5, 2.5 and 5.0) have higher visible light response than the NT/TiO_2. Among the electrode modified with tungsten, NT/Ti-5.0W presented the best photocatalytic activity, with current densities around of 1.0 and 2.2mA cm^{-2} at 0.8V *vs*. Ag/AgCl under UV-Vis and Visible irradiation, respectively, which are 376 % and 70 % more than NT/TiO_2at same conditions.

Comparing the results of **Figure 7a-b**, it is noticed that in the presence of gap acceptors the performance of all modified electrodes was notable, showing a rapid increase in current density

in the low potential region, and then reaching saturation with an increase in the potential applied. This behavior was observed in both UV-Vis and visible light, indicating that NT/Ti-xW films easily interact at the interface with the gap acceptor, suggesting that they are promising in the decomposition of organic pollutants based on photocatalytic and photoelectrocatalytic processes [66].

3.3 Photocatalytic activity of the nanotubular oxides at hormones degradation

To compare the photocatalytic activity among the electrodes modified with tungsten (NT/Ti-xW, x = 0.5, 2.5 and 5.0) and no modified (NT/TiO_2), working solutions of E1 and EE2 were degraded by five processes under UV-vis light: direct photolysis, photocatalysis (PC) and photoelectrocatalysis (PEC). For every experimental run, the adsorption equilibrium between the catalyst and the hormone was achieved under dark by mixing of the solution during 5 min, before switching on the light of the photodegradation system. As shown in **Fig. 8a** and **b**, the performance of the electrodes modified with tungsten (NT/Ti-xW, x = 0.5, 2.5 and 5.0) in the E1 and EE2 degradation was better than that with NT/TiO_2 for both processes (PC and PEC).

For photolysis, the degradation was much faster for E1, which was 35.2 % converted after 2 min, while for EE2 no conversion occurred. It can be explained by the stronger absorption of photons for E1 in the UV region, which is in agreement with the results reported for single and multicomponent solution of estrogens containing E1 [86]

For the photocatalysis processes, the nanotubes with low W content showed higher degradation efficiency for E1 while for EE2 the best degradation was obtained with the nanotubes with high W content. In these conditions, the degradation of the estrogens was around 48.6% at 2 min. According to NT/Ti-0.5W electrode characterization studies published by [44], the position of the CB and VB edges of the NT/Ti0.5W, which are located at -0.26 V and +2.65 V *vs*. NHE (pH 7), respectively, are favorable to formation of superoxide radical anion $^{\bullet}O_2^-$ (CB)and hydroxyl radical •OH (VB), due to the position of the standard redox potential of the $O_2/^{\bullet}O_2^-$ (−0.18 V vs NHE, pH 7) and $OH^-/^{\bullet}OH$ (1.99 V *vs* NHE, pH 7) couples [87], as illustrated in **Fig. 9a**. Then, the E1 hormone can be degraded for these both oxidants. On the other hand, for NT/Ti5.0W electrode where the presence of WO_3 (W^{6+}) in the oxide nanotubular wall was also evidenced by XPS and Raman analysis, the formation of superoxide radical anion $^{\bullet}O_2^-$ is decreased because the electrons transferred from W doped TiO_2 CB and trapped as W^{5+} sites cannot be transferred to O_2 molecular due to the lower position of CB edge of WO_3 (+0.25V) in relation of the standard redox potential $O_2/^{\bullet}O_2^-$ (−0.18 V *vs*. NHE, pH 7), as shown in **Fig. 9b**. In addition, the electrons photogenerated may easily be recombined with photogenerated holes, reducing of E1 degradation efficiency. However, in the case of EE2, its degradation under acid conditions (pH 3) takes place preferentially by the attack of the hydroxyl radical [20], which can be produced both regions, rich

in WO_3 and in those with W doped TiO_2 (**Fig. 9b**), thus justifying the greater efficiency of the NT/Ti-5W electrode in the degradation of EE2.

On the other hand, for photoelectrocatalytic process the NT/Ti-5.0W promoted the highest degradation efficiency for both hormones. Under the same experimental conditions, the amount of E1 and EE2 degraded in 2.0min with PEC using NT/Ti-5.0W was 1.4 and 1.3 times that with NT/Ti-0.5W, as seen in **Fig. 8a** and **b**. In relation to NT/TiO_2, this increase corresponds to 4.2 times. When an anodic bias is applied on the photocatalytic process the separation of electron-holes is accelerated, increasing the transport of the holes to the surface and the electrons away from the surface (direction to inside of the electrode). Consequently, there is a decrease in the charge recombination rate (electron-hole) and an increase in the generation of hydroxyl radicals ($^{\bullet}OH$) on the NT/Ti-5.0W (**Fig. 9c**). Although in the NT/Ti-0.5W sample there is also a reduction in the recombination rate, the amount $^{\bullet}O_2$- generated is significantly reduced due to the electron flow towards the counter-electrode, reducing its photocatalytic performance.

The high performance of the NT/Ti-5.0W electrode can also be attributed to the following factors: high concentration of W^{+6} that acts as mediators for charge transfer to the solution and greater acidity of the sample due to the presence of WO_3. Studies reported in the literature showed that when loading up to 3% mol of WO_3 onto TiO_2 nanoparticles, the Lewis surface acidity is increased up to a factor of 15, contributing to improve the adsorption of OH^- or H_2O on the catalyst surface and, consequently, generate a greater amount of $^{\bullet}OH$ radical. At the same time, it can adsorb more organic compounds [88].

Among the electrodes modified with W content, the NT/Ti-2.5W presented the worst degradation results, independent of the process used. Many factors may have contributed to its low performance. Among them, we can highlight:

a) high amount of W^{+5} in the oxide layer (Table 2). According to [53] W^{+5} favors binding with the ^-OH from water over binding the hormone, so the efficiency of hormone degradation is compromised for the alloy with the highest amount of W^{+5}.

b) high density of oxygen vacancy or defects that result in an increase in the number of charge recombination centers. This phenomenon is evidenced by its greater intensity of green emission in the photoluminescence study and corroborated by the XPS analysis, where the amount of W^{+5} is greater.

c) low concentration of WO_3 (W^{+6}) that could reduce the effect of photogenerated charge recombination centers caused by excess oxygen vacancy or defects by formation of heterojunction.

Taking in account the better performance of the NT/Ti-xW samples in EE2 and E1 degradation under UV-Vis, photoelectrocatalytic experiments under visible light were carried out using NT/Ti-0.5W e NT/Ti-5W, and the results compared with NT/TiO_2, as shown in **Fig.8c** e **d**. For short time degradation, the NT/Ti-5W proved to be more efficient while for longer times,

higher degradation efficiencies were obtained with the doped sample (NT/Ti-0.5W). This result can be explained by the loss of stability of WO_3 present in oxide layer of NT/Ti-5W, as suggested by Das and co-authors [31]. Knöppel and co-authors [89] demonstrated that in the absence of light, WO_3 is stable in a wide potential range, but in the presence of light, it dissolves proportionally to the anodic photocurrent due to the formation of aqueous tungsten complexes with the electrolyte that are thermodynamically more stable than WO_3. In general, the leaching process is accelerated with the use of S-containing electrolyte anions because it reacts with WO_3 to form stable complexes (persulfate intermediates), reducing the photostability of WO_3 photoelectrodes [90]. Considering that pure water was used as electrolyte in the hormone degradation experiments, probably, with the progress of the decomposition reaction of EE2, by-products were produced and formed complex with W^{6+} that are more stable than WO_3, resulting in the WO_3 leaching. This consideration can be confirmed by **Fig 9d** where a significant reduction in visible absorption is observed after 8 h of EE2 degradation, as well as in the UV region, probably due to adsorption of formed by-products, reducing the active area of the electrode. The leaching phenomenon occurred because WO_3 was not inserted in the TiO_2 crystal lattice. As discussed earlier, it was obtained from the precipitated W and Ti-β phase formed during the confection of metallic substrate. In the case of NT/Ti-0.5W, all W content is inserted in the TiO_2 crystal lattice, avoiding the material corrosion, and favoring your best performance for long time degradation.

3.4 Hormones Degradation in real water matrix

Finally, the electrodes modified with tungsten (NT/Ti-xW, x = 0.5, 2.5 and 5.0) and no modified (NT/TiO_2) were used to evaluate the degradation of E1 and EE2 in real water supply source under photoelectrocatalytic process and UV-Vis radiation. The real water matrix, with a total carbon organic of 577.4 ppm (**Table S1**), and a pH 7.0, was spiked with 10 mg L^{-1} of E1 and EE2 each. Although, the concentrations of the hormones in natural aquatic environmental are in ng L^{-1} range (5900 ng L^{-1} and 1800 ng L^{-1} for EE2 and E1, respectively), it is important to understand the effect of this matrix in the degradation experiments. The results (**Fig. 10**) showed that due to the complexity of the real water matrix the time for degradation 50% of E1 and EE2 was substantially higher, 8.7 and 27.4 times more, respectively, than using the solution without competitive chemicals. This reduction of degradation efficiency of the hormones can be associated to the presence of hydroxyl radical scavengers, such as organic matter or inorganic anions, chloride, bicarbonate and sulfate [91].Besides the adsorption of some inorganic ions or other substance dissolved in the water matrix can be adsorbed on the photocatalyst, reducing the number of sites which could be available to the estrogens degradation, as observed by [92,93]. In addition, the real matrix was a little turbid which can be contributed for reduction of the photon

flux absorbed by the photocatalyst. Similar behavior was also observed in other studies of hormones degradation using different matrices [92,94,95].

For both hormones, the degradation efficiency was higher with NT/Ti-5.0W electrode. In the case of E1 degradation, a very fast degradation is observed in the first 15 - 20 min of treatment, remaining constant during a long time and falling again in the last 15 min. During the E1 degradation process, the formation of two secondary peaks occurred in the chromatogram, called X and Y, as shown in **Fig. 11**. When the concentration of these by-products becomes significant, the E1 degradation rate continues to occur but at a very slow rate. Only after the almost complete degradation of these by-products, the degradation rate of E1 increases again. This phenomenon was observed for all samples, but it was more evident with the NT/Ti-5.0W sample. Regarding the EE2 degradation, it was observed a continuous decay in the concentration of this hormone for all samples, and similar to that obtained with the synthetic solution, reaching 77.9% of EE2 degradation using NT/Ti-5.0W in 60 min. Based on previous work [44] using NT/Ti-0.5W for E1 and EE2 photoelectrocatalytic degradation, oxalic acid and glutaric acid are the possible products obtained from estrone degradation after 60 min of photoelectrocatalytic treatment. While for the EE2, the possible by-products formed were oxalic acid, malonic acid, glutaric acid, and the intermediates compounds (2-OH-EE2, 6-OH-EE2, and compound at m/z 328).

The results of E1 and EE2 degradation using PEC under UV-Vis were adjusted with the simplest approach of Langmuir-Hinshelwood model and expressed by the following equation (3).

$$r = -\frac{dC}{dt} = \frac{k \cdot K \cdot C}{1 + K \cdot C} \quad (3)$$

where k is the reaction rate constant, K the adsorption-desorption equilibrium constant and C is the concentration of the organic pollutant. Considering the low hormone concentrations and adsorption-desorption tests carried out in the dark for all electrodes for NT/Ti-xW (Figure S6), the $K \cdot C <<< 1$, this equation is arranged, assuming the first-order kinetic model, as equations (4) and (5) below:

$$-\frac{dC}{dt} = k_{(app)} \cdot C \quad (4)$$

$$-\ln\frac{C(t)}{C(0)} = k_{(app)} \cdot t \quad (5)$$

where $C(0)$ and $C(t)$ are the concentrations at time zero and time (t), and $k_{(app)}$ is the apparent first-order degradation rate constant. The results in Table 2 indicate that the kinetics of the photodegradation are in accord with the model proposed, with correlation coefficients > 0.9 and presented acceptable values of χ^2 (5 degrees of freedom, $\alpha = 0.05$, which have a critical value of 1.145). A promising E1 degradation rate was obtained with NT/Ti-5.0W with a value two and

three times higher than that obtained with other alloys and NT/TiO_2, respectively. On the other hand, only small increases were observed in the EE2 degradation rate with increasing amount of W in the electrode. In general, the increasing in removal rate of EE2 is less pronounced than that of E1, because it is more stable in the different environmental which is the main characteristic of synthetic hormones. The rate of EE2 degradation obtained in this work using real water matrix and the NT/Ti-5.0W electrode ($k = 0.025\ min^{-1}$) was slightly higher than that found by Nasuhoglu et al. [96] using TiO_2 suspension irradiated with a UV radiation and real wastewater ($k = 0.022\ min^{-1}$).

DRS analysis carried out before and after EE2 degradation demonstrated a reduction in the intensity of UV and visible light absorption as shown in **Fig.12**. Probably this is due to adsorption of some inorganic ions or other substance dissolved in the water matrix and the WO_3 leaching, as observed earlier after the tests under visible radiation. But for the NT/Ti-0.5W and NT/Ti-2.5 W samples, no or only a small change was observed, evidencing the greater stability of these electrodes in relation to the electrode with higher W content.

Although it took a longer time for the degradation of the E1 and EE2 hormones in the real matrix, the photocatalysts evaluated in this work showed certain selectivity towards to the hormones in relation to other compounds present in the aqueous medium. Only a TOC reduction of 7.6 and 14.5% was achieved after 20 and 50 min, respectively, of EE2 photoelectrocatalytic treatment using NT/Ti5.0Win real water matrix (**Table S1**).

Stability tests using PEC and real water matrix under UV-Vis and visible light for 1 and 8 h showed only small oscillations in the current values for all photoelectrodes, indicating the stability and applicability of these materials in real medium (Fig. S7).

3. **Conclusions**

The production and photocatalytic performance of the nanotubes grown on Ti-W alloy is strongly dependent of the W content in the substrate. By Rietveld refinement method, Ti-α and doped Ti-α phases were identified in Ti-0.5W(wt.%), while Ti-β phase and W precipitate were also obtained in Ti-2.5W(wt.%) and Ti-5.0W(wt.%), but in higher quantity in the last sample. In order to produce the nanotubular oxide layer on the alloys with similar dimensions, more time of anodization was required to the substrates with higher W content under 120 V. During the heat treatment of the oxide film, it was observed that the increasing W content stabilizes the anatase phase, delaying the appearance of the rutile phase [97]. Therefore, heat treatment temperature of 550 °C was necessary to obtain higher photocurrent values with the increase in the amount of W in the oxide layer.

XRD data revealed the formation of non-stoichiometric oxides (WO_{3-x} ($0 \leq x \leq 0.28$)) and ternary oxide ($Ti_{0.54}W_{0.46}O_2$) for samples with higher amounts of tungsten in the alloy. These

results corroborated with the XPS studies that also revealed the presence of oxidative species W^{4+}, W^{5+} and W^{6+} from these oxides. The predominance of W^{5+} was clearly observed for the NT/Ti-0.5W and NT/Ti-2.5W films, while the percentage of W^{6+} was higher for the NT/Ti-5.0W sample. The characterizations of NT/Ti-xW films also showed that the W^{4+} species can be attributed to the ternary oxide coming from the solid solution present in the substrate. The W^{5+} species is referred to oxygen vacancies and its formation was conducted from the interstitial doping originated by the metastable Ti-β phase. Meanwhile, the presence of WO_3 in the composition of the nanotubular matrix had a W precipitate as precursor. Then, the metallic substrate acted as precursor in the formation of the oxide film.

The optical properties of modified nanotubular matrices were strongly influenced by tungsten species and oxygen vacancies, characterizing them as important semiconductors with low recombination rate and significant absorption in the visible spectrum, mainly observed for the NT/Ti-5.0W film. The insertion of intermediate levels through the oxidative species of W in the TiO_2 bandgap favored the electronic transition and longer lifetime of the photogenerated charges. This has been observed in the comparison of photoelectrocatalytic efficiencies between nanotubes grown on Ti-W alloys and pure NT/TiO_2.

Higher degradation efficiencies of E1 and EE2 were reached with NT/Ti-5.0W electrode for both matrices, pure and real supply water, under photoelectrocatalytic process and UV-Vis irradiation. But the time for degradation of 50 % of E1 and EE2 in the real water matrix was substantially higher, 8.7 and 27.4 times more, than that of the solution without competitive chemicals. This reduction of efficiency degradation may be associated with the water turbidity and the presence of some inorganic ions and/or organic substance present in the matrix, which act as hydroxyl radical scavengers. Mineralization of the pollutant in the real water matrix was less than 15 % after 50 min of photoelectrocatalytic treatment suggesting a certain selectivity of the photocatalyst towards the hormones in relation to other compounds in the aqueous medium. The high performance of the NT/Ti-5.0W was associated with the combination of doping (W doped TiO_2) and heterojunction (WO_3 (W^{6+})) process, while for other electrodes (NT/Ti-0.5 and NT/2.5W) the doping process was predominant. However, the stability of this electrode was compromised under long degradation times, mainly under visible light, probably due to a WO_3 leaching process, because of its non-anchoring in the TiO_2 crystal lattice.

Acknowledgments

The authorsthank FAPESP – Fundação de Amparo à Pesquisa do Estado de São Paulo (ProcessNumber06/61261–2and 2014/50945-4), and CNPq – Conselho Nacional de Desenvolvimento Científico e Tecnológico (ProcessNumber483285/2011–0and 465571/2014-0) for financial support. Thisstudywasalsofinanced in partbythe Coordenação de Aperfeiçoamento

de Pessoal de Nível Superior – Brasil (CAPES) – FinanceCode 001. This research used facilities of the Brazilian Nanotechnology National Laboratory (LNNano), part of the Brazilian Centre for Research in Energy and Materials (CNPEM), a private non-profit organization under the supervision of the Brazilian Ministry for Science, Technology, and Innovations (MCTI). The (SEM-FEG and XPS) staff is acknowledged for the assistance during the experiments (proposal numbersSEM-20059 and XPS-21555). The authors acknowledge the support of Núcleo de Instrumentação para Pesquisa e Ensino (NIPE) of the Centro de Equipamentos e Serviços Multiusuários (CESM-ICAQF) of UNIFESP – Campus Diadema for the Raman, DRS and XRD characterization techniques and, LENCA – Laboratório de Engenharia e Controle Ambiental for chromatographic analyses. The authors are grateful to the Prof. Máximo Siu Li (IFSC - USP/São Carlos) for the photoluminescence and Prof. Richard Landers (IFGW – UNICAMP) with the collaboration with the XPS characterization.

References

[1] M. Adeel, X. Song, Y. Wang, D. Francis, Y. Yang, Environmental impact of estrogens on human, animal and plant life: A critical review, Environ. Int. 99 (2017) 107–119. doi:10.1016/j.envint.2016.12.010.

[2] C.N. Rani, S. Karthikeyan, Endocrine disrupting compounds in water and wastewater and their treatment options - A review, Int. J. Environ. Technol. Manag. 19 (2016) 392–431. doi:10.1504/IJETM.2016.083660.

[3] A.Z. Aris, A.S. Shamsuddin, S.M. Praveena, Occurrence of 17α-ethynylestradiol (EE2) in the environment and effect on exposed biota: A review, Environ. Int. 69 (2014) 104–119. doi:10.1016/j.envint.2014.04.011.

[4] K. Volkova, N. Reyhanian Caspillo, T. Porseryd, S. Hallgren, P. Dinnetz, H. Olsén, I. Porsch Hällström, Transgenerational effects of 17α-ethinyl estradiol on anxiety behavior in the guppy, Poecilia reticulata, Gen. Comp. Endocrinol. 223 (2015) 66–72. doi:10.1016/j.ygcen.2015.09.027.

[5] K. Wojnarowski, P. Podobiński, P. Cholewińska, J. Smoliński, K. Dorobisz, Impact of estrogens present in environment on health and welfare of animals, Animals. 11 (2021) 1–16. doi:10.3390/ani11072152.

[6] Å. Bergman, J. Heindel, S. Jobling, K. Kidd, R.T. Zoeller, State of the science of endocrine disrupting chemicals 2012: an assessment of the state of the science of endocrine disruptors prepared by a group of experts for the United Nations Environment Programme and World Health Organization, 2013. doi:10.1016/j.toxlet.2012.03.020.

[7] T. Heberer, Occurrence, fate, and removal of pharmaceutical residues in the aquatic

environment: a review of recent research data, Toxicol. Lett. 131 (2002) 5–17. doi:10.1016/S0378-4274(02)00041-3.

[8] J.W. Birkett, J.N. Lester, Endocrime Disrupters in Wastewater and Sludge Treatment Process, 1991. doi:10.1016/0015-1882(91)80016-X.

[9] A.J. Ebele, M. Abou-Elwafa Abdallah, S. Harrad, Pharmaceuticals and personal care products (PPCPs) in the freshwater aquatic environment, Emerg. Contam. 3 (2017) 1–16. doi:10.1016/j.emcon.2016.12.004.

[10] C.C. Montagner, C. Vidal, R.D. Acayaba, Contaminantes emergentes em matrizes aquáticas do Brasil: Cenário atual e aspectos analíticos, ecotoxicológicos e regulatórios, Quim. Nova. 40 (2017) 1094–1110. doi:10.21577/0100-4042.20170091.

[11] G.P. Pessoa, N.C. de Souza, C.B. Vidal, J.A.C. Alves, P.I.M. Firmino, R.F. Nascimento, A.B. dos Santos, Occurrence and removal of estrogens in Brazilian wastewater treatment plants, Sci. Total Environ. 490 (2014) 288–295. doi:10.1016/j.scitotenv.2014.05.008.

[12] Y. Luo, W. Guo, H.H. Ngo, L.D. Nghiem, F.I. Hai, J. Zhang, S. Liang, X.C. Wang, A review on the occurrence of micropollutants in the aquatic environment and their fate and removal during wastewater treatment, Sci. Total Environ. 473–474 (2014) 619–641. doi:10.1016/j.scitotenv.2013.12.065.

[13] M. Taheran, S.K. Brar, M. Verma, R.Y. Surampalli, T.C. Zhang, J.R. Valero, Membrane processes for removal of pharmaceutically active compounds (PhACs) from water and wastewaters, Sci. Total Environ. 547 (2016) 60–77. doi:10.1016/j.scitotenv.2015.12.139.

[14] S.O. Ganiyu, E.D. Van Hullebusch, M. Cretin, G. Esposito, M.A. Oturan, Coupling of membrane filtration and advanced oxidation processes for removal of pharmaceutical residues: A critical review, Sep. Purif. Technol. 156 (2015) 891–914. doi:10.1016/j.seppur.2015.09.059.

[15] J.C. Carlson, M.I. Stefan, J.M. Parnis, C.D. Metcalfe, Direct UV photolysis of selected pharmaceuticals, personal care products and endocrine disruptors in aqueous solution, Water Res. 84 (2015) 350–361. doi:10.1016/j.watres.2015.04.013.

[16] M.M. Huber, A. Göbel, A. Joss, N. Hermann, D. Löffler, C.S. McArdell, A. Ried, H. Siegrist, T.A. Ternes, U. Von Gunten, Oxidation of pharmaceuticals during ozonation of municipal wastewater effluents: A pilot study, Environ. Sci. Technol. 39 (2005) 4290–4299. doi:10.1021/es048396s.

[17] Y. Yang, Y.S. Ok, K.H. Kim, E.E. Kwon, Y.F. Tsang, Occurrences and removal of pharmaceuticals and personal care products (PPCPs) in drinking water and water/sewage treatment plants: A review, Sci. Total Environ. 596–597 (2017) 303–320.

doi:10.1016/j.scitotenv.2017.04.102.

[18] P. Westerhoff, Y. Yoon, S. Snyder, E. Wert, Fate of endocrine-disruptor, pharmaceutical, and personal care product chemicals during simulated drinking water treatment processes, Environ. Sci. Technol. 39 (2005) 6649–6663. doi:10.1021/es0484799.

[19] P. Roy, S. Berger, P. Schmuki, TiO_2 nanotubes: Synthesis and applications, Angew. Chemie - Int. Ed. 50 (2011) 2904–2939. doi:10.1002/anie.201001374.

[20] W. Sun, S. Li, J. Mai, J. Ni, Initial photocatalytic degradation intermediates/pathways of 17α-ethynylestradiol: Effect of pH and methanol, Chemosphere. 81 (2010) 92–99. doi:10.1016/j.chemosphere.2010.06.051.

[21] C.W. Lai, S. Sreekantan, Photoelectrochemical performance of smooth TiO 2 nanotube arrays: Effect of anodization temperature and cleaning methods, Int. J. Photoenergy. 2012 (2012). doi:10.1155/2012/356943.

[22] K. Lee, A. Mazare, P. Schmuki, One-Dimensional Titanium Dioxide Nanomaterials: Nanotubes, Chem. Rev. 114 (2014) 9385–9454. doi:10.1021/cr500061m.

[23] K. Nishijima, T. Kamai, N. Murakami, T. Tsubota, T. Ohno, Photocatalytic Hydrogen or Oxygen Evolution from Water over S- or N-Doped TiO 2 under Visible Light , Int. J. Photoenergy. 2008 (2008) 1–7. doi:10.1155/2008/173943.

[24] L.C. Almeida, M.V.B. Zanoni, Decoration of Ti/TiO 2 Nanotubes with Pt Nanoparticles for Enhanced UV-Vis Light Absorption in Photoelectrocatalytic Process, J. Braz. Chem. Soc. 25 (2014) 579–588. doi:10.5935/0103-5053.20140034.

[25] S.K. Mohapatra, S.E. John, S. Banerjee, M. Misra, Water photooxidation by smooth and ultrathin R-Fe2O3 nanotube arrays, Chem. Mater. 21 (2009) 3048–3055. doi:10.1021/cm8030208.

[26] N. Lu, X. Quan, J.Y. Li, S. Chen, H.T. Yu, G. Chen, Fabrication of boron-doped TiO2 nanotube array electrode and investigation of its photoelectrochemical capability, J. Phys. Chem. C. 111 (2007) 11836–11842. doi:10.1021/jp071359d.

[27] A.S. Martins, P.J.M. Cordeiro-Junior, L. Nuñez, M.R. de V. Lanza, A Simple Method for the Electrodeposition of WO3 in TiO2 Nanotubes: Influence of the Amount of Tungsten on Photoelectrocatalytic Activity, Electrocatalysis. 8 (2017) 115–121. doi:10.1007/s12678-016-0335-9.

[28] M.V. Dozzi, S. Marzorati, M. Longhi, M. Coduri, L. Artiglia, E. Selli, Photocatalytic activity of TiO_2-WO_3 mixed oxides in relation to electron transfer efficiency, Appl. Catal. B Environ. 186 (2016) 157–165. doi:10.1016/j.apcatb.2016.01.004.

[29] H. Il Kim, J. Kim, W. Kim, W. Choi, Enhanced photocatalytic and photoelectrochemical

activity in the ternary hybrid of CdS/TiO2/WO3 through the cascadal electron transfer, J. Phys. Chem. C. 115 (2011) 9797–9805. doi:10.1021/jp1122823.

[30] S. Higashimoto, M. Sakiyama, M. Azuma, Photoelectrochemical properties of hybrid WO3/TiO2 electrode. Effect of structures of WO3 on charge separation behavior, Thin Solid Films. 503 (2006) 201–206. doi:10.1016/j.tsf.2005.11.110.

[31] C. Das, I. Paramasivam, N. Liu, P. Schmuki, Photoelectrochemical and photocatalytic activity of tungsten doped TiO_2 nanotube layers in the near visible region, Electrochim. Acta. 56 (2011) 10557–10561. doi:10.1016/j.electacta.2011.05.061.

[32] I. Paramasivam, Y.C. Nah, C. Das, N.K. Shrestha, P. Schmuki, WO_3/TiO_2 nanotubes with strongly enhanced photocatalytic activity, Chem. - A Eur. J. 16 (2010) 8993–8997. doi:10.1002/chem.201000397.

[33] M. Kang, J. Liang, F. Wang, X. Chen, Y. Lu, J. Zhang, Structural design of hexagonal/monoclinic WO3 phase junction for photocatalytic degradation, Mater. Res. Bull. 121 (2020) 110614. doi:10.1016/j.materresbull.2019.110614.

[34] H. Yoo, K. Oh, Y.C. Nah, J. Choi, K. Lee, Single-Step Anodization for the Formation of WO3-Doped TiO2 Nanotubes Toward Enhanced Electrochromic Performance, ChemElectroChem. 5 (2018) 3379–3382. doi:10.1002/celc.201800981.

[35] X. Wang, M. Sun, M. Murugananthan, Y. Zhang, L. Zhang, Electrochemically self-doped WO3/TiO2 nanotubes for photocatalytic degradation of volatile organic compounds, Appl. Catal. B Environ. 260 (2020) 118205. doi:10.1016/j.apcatb.2019.118205.

[36] W. Huang, J. Wang, L. Bian, C. Zhao, D. Liu, C. Guo, B. Yang, W. Cao, Oxygen vacancy induces self-doping effect and metalloid LSPR in non-stoichiometric tungsten suboxide synergistically contributing to the enhanced photoelectrocatalytic performance of WO3-:X/TiO2-x heterojunction, Phys. Chem. Chem. Phys. 20 (2018) 17268–17278. doi:10.1039/c8cp02044b.

[37] J. Liu, Y. Li, J. Ke, S. Wang, L. Wang, H. Xiao, Black NiO-TiO2 nanorods for solar photocatalysis: Recognition of electronic structure and reaction mechanism, Appl. Catal. B Environ. 224 (2018) 705–714. doi:10.1016/j.apcatb.2017.11.028.

[38] Y. Shabdan, A. Markhabayeva, N. Bakranov, N. Nuraje, Photoactive tungsten-oxide nanomaterials for water-splitting, Nanomaterials. 10 (2020) 1–37. doi:10.3390/nano10091871.

[39] I. Tsangaraki-Kaplanoglou, S. Theohari, T. Dimogerontakis, Y.M. Wang, H.H. Kuo, S. Kia, Effect of alloy types on the anodizing process of aluminum, Surf. Coatings Technol. 200 (2006) 2634–2641. doi:10.1016/j.surfcoat.2005.07.065.

[40] J. de Almeida, S.H. Câmara, R. Bertazzoli, R.G. Silva, C.A. Rodrigues, Synthesis and Characterization of Self-Organized Oxide Layer Grown on Ti-Cu Alloys System for CO 2 Reduction , ECS Trans. 89 (2019) 45–51. doi:10.1149/08907.0045ecst.

[41] M. Gies, F. Michel, C. Lupó, D. Schlettwein, M. Becker, A. Polity, Electrochromic switching of tungsten oxide films grown by reactive ion-beam sputter deposition, J. Mater. Sci. 56 (2021) 615–628. doi:10.1007/s10853-020-05321-y.

[42] G. Zheng, J. Wang, H. Liu, V. Murugadoss, G. Zu, H. Che, C. Lai, H. Li, T. Ding, Q. Gao, Z. Guo, Tungsten oxide nanostructures and nanocomposites for photoelectrochemical water splitting, Nanoscale. 11 (2019) 18968–18994. doi:10.1039/c9nr03474a.

[43] R. Wu, J. Zhang, Y. Shi, D. Liu, B. Zhang, Metallic WO2-Carbon Mesoporous Nanowires as Highly Efficient Electrocatalysts for Hydrogen Evolution Reaction, J. Am. Chem. Soc. 137 (2015) 6983–6986. doi:10.1021/jacs.5b01330.

[44] M. de O. Escudeiro, B.L. Barroso, J. De Almeida, M.L.L. Moraes, C. de Arruda Rodrigues, Photoelectrocatalytic degradation of 17α-ethinylestradiol and estrone under UV and visible light using nanotubular oxide arrays grown on Ti-0.5wt%W, Environ. Res. 191 (2020) 110044. doi:10.1016/j.envres.2020.110044.

[45] L.H.G. Coelho, T.A. de Jesus, M.Y. Kohatsu, G.T. Poccia, V. Chicarolli, K. Helwig, C. Hunter, J. Roberts, P. Teedon, O. Pahl, Estrogenic Hormones in São Paulo Waters (Brazil) and Their Relationship with Environmental Variables and Sinapis alba Phytotoxicity, Water. Air. Soil Pollut. 231 (2020). doi:10.1007/s11270-020-04477-2.

[46] J.L. Murray, The Ti-W (Titanium-Tungsten) system, Bull. Alloy Phase Diagrams. 2 (1981) 192–196. doi:10.1007/BF02881477.

[47] R.B. da Silva, W.S. Hanisch, Modelagem do fenômeno de floração de cianobactérias por meio de redes neurais artificiais na captação da represa Guarapiranga, Universidade Federal de São Paulo, 2017.

[48] A.S.M. International, ASM METALS HANDBOOK VOLUME 3 Alloy Phase Diagrams, n.d.

[49] J.C. Slater, Atomic radii in crystals, J. Chem. Phys. 41 (1964) 3199–3204. doi:10.1063/1.1725697.

[50] H. Tsuchiya, T. Akaki, J. Nakata, D. Terada, N. Tsuji, Y. Koizumi, Y. Minamino, P. Schmuki, S. Fujimoto, Metallurgical aspects on the formation of self-organized anodic oxide nanotube layers, Electrochim. Acta. 54 (2009) 5155–5162. doi:10.1016/j.electacta.2009.02.038.

[51] A. Watcharenwong, W. Chanmanee, N.R. de Tacconi, C.R. Chenthamarakshan, P.

Kajitvichyanukuk, K. Rajeshwar, Self-organized TiO2 nanotube arrays by anodization of Ti substrate: Effect of anodization time, voltage and medium composition on oxide morphology and photoelectrochemical response, J. Mater. Res. 22 (2007) 3186–3195. doi:10.1557/jmr.2007.0391.

[52] H. Slimen, A. Houas, J.P. Nogier, Elaboration of stable anatase TiO2 through activated carbon addition with high photocatalytic activity under visible light, J. Photochem. Photobiol. A Chem. 221 (2011) 13–21. doi:10.1016/j.jphotochem.2011.04.013.

[53] P.J. Boruah, R.R. Khanikar, H. Bailung, Synthesis and Characterization of Oxygen Vacancy Induced Narrow Bandgap Tungsten Oxide (WO3−x) Nanoparticles by Plasma Discharge in Liquid and Its Photocatalytic Activity, Plasma Chem. Plasma Process. 40 (2020) 1019–1036. doi:10.1007/s11090-020-10073-3.

[54] D. Sivkov, S. Nekipelov, O. Petrova, A. Vinogradov, A. Mingaleva, S. Isaenko, P. Makarov, A. Ob'edkov, B. Kaverin, S. Gusev, I. Vilkov, A. Aborkin, V. Sivkov, Studies of buried layers and interfaces of tungsten carbide coatings on the MWCNT surface by XPS and NEXAFS spectroscopy, Appl. Sci. 10 (2020). doi:10.3390/app10144736.

[55] S. Chen, Y. Xiao, W. Xie, Y. Wang, Z. Hu, W. Zhang, H. Zhao, Facile strategy for synthesizing non-stoichiometric monoclinic structured tungsten trioxide (WO3−x) with plasma resonance absorption and enhanced photocatalytic activity, Nanomaterials. 8 (2018). doi:10.3390/nano8070553.

[56] J. Singh, S.S. Sharma, S.S. Sharma, R.C. Singh, Effect of tungsten doping on structural and optical properties of rutile TiO 2 and band gap narrowing, Optik (Stuttg). 182 (2019) 538–547. doi:10.1016/j.ijleo.2019.01.070.

[57] E. Peters, H. Muller-Buschbaum, On a Low Valent Titanium Tungsten Oxide: Ti0.54W0.46O2, Z. Naturforsch. 51b (1996) 29–31. doi:10.1515/znb-1996-0107.

[58] A.K.L. Sajjad, S. Shamaila, B. Tian, F. Chen, J. Zhang, One step activation of WOx/TiO_2 nanocomposites with enhanced photocatalytic activity, Appl. Catal. B Environ. 91 (2009) 397–405. doi:10.1016/j.apcatb.2009.06.005.

[59] L. Gao, W. Gan, Z. Qiu, X. Zhan, T. Qiang, J. Li, Preparation of heterostructured WO3/TiO2 catalysts from wood fibers and its versatile photodegradation abilities, Sci. Rep. 7 (2017). doi:10.1038/s41598-017-01244-y.

[60] G.L. Frey, A. Rothschild, J. Sloan, R. Rosentsveig, R. Popovitz-Biro, R. Tenne, Investigations of nonstoichiometric tungsten oxide nanoparticles, J. Solid State Chem. 162 (2001) 300–314. doi:10.1006/jssc.2001.9319.

[61] A.R. Luz, L.S. Santos, C.M. Lepienski, P.B. Kuroda, N.K. Kuromoto, Characterization of

the morphology, structure and wettability of phase dependent lamellar and nanotube oxides on anodized Ti-10Nb alloy, Appl. Surf. Sci. 448 (2018) 30–40. doi:10.1016/j.apsusc.2018.04.079.

[62] D. Georgescu, L. Baia, O. Ersen, M. Baia, S. Simon, Experimental assessment of the phonon confinement in TiO2 anatase nanocrystallites by Raman spectroscopy, J. Raman Spectrosc. 43 (2012) 876–883. doi:10.1002/jrs.3103.

[63] J. Kunze, A. Seyeux, P. Schmuki, Anodic TiO_2 layer conversion: Fluoride-induced rutile formation at room temperature, Electrochem. Solid-State Lett. 11 (2008) 2007–2009. doi:10.1149/1.2811722.

[64] Z. Sadighi, J. Huang, L. Qin, S. Yao, J. Cui, J.K. Kim, Positive role of oxygen vacancy in electrochemical performance of CoMn2O4 cathodes for Li-O2 batteries, J. Power Sources. 365 (2017) 134–147. doi:10.1016/j.jpowsour.2017.08.081.

[65] H.C. Chen, D.J. Jan, Y.S. Luo, K.T. Huang, Electrochromic and optical properties of tungsten oxide films deposited with DC sputtering by introducing of hydrogen, Opt. InfoBase Conf. Pap. 53 (2013) 321–329. doi:10.1364/ao.53.00a321.

[66] Y.K. Hsu, Y.C. Chen, Y.G. Lin, L.C. Chen, K.H. Chen, Birnessite-type manganese oxides nanosheets with hole acceptor assisted photoelectrochemical activity in response to visible light, J. Mater. Chem. 22 (2012) 2733–2739. doi:10.1039/c1jm14355g.

[67] C.D. Wagner, W.M. Riggs, L.E. Davis, J.F. Moulder, G.E. Muilenberg, Handbook of X Ray Photoelectron Spectroscopy: A Reference Book of Standard Spectra for Identification and Interpretation of XPS Data, First Edit, Perkin-Elmer Corporation Physical Electonics Division, Eden Praire, Minnesota, 1979.

[68] L. Yang, Y. Xiao, S. Liu, Y. Li, Q. Cai, S. Luo, G. Zeng, Photocatalytic reduction of Cr(VI) on WO3 doped long TiO2 nanotube arrays in the presence of citric acid, Appl. Catal. B Environ. 94 (2010) 142–149. doi:10.1016/j.apcatb.2009.11.002.

[69] S.Q. Yu, Y.H. Ling, R.G. Wang, J. Zhang, F. Qin, Z.J. Zhang, Constructing superhydrophobic WO3@TiO2 nanoflake surface beyond amorphous alloy against electrochemical corrosion on iron steel, Appl. Surf. Sci. 436 (2018) 527–535. doi:10.1016/j.apsusc.2017.11.211.

[70] A. Kafizas, I.P. Parkin, Combinatorial atmospheric pressure chemical vapor deposition (cAPCVD): A route to functional property optimization, J. Am. Chem. Soc. 133 (2011) 20458–20467. doi:10.1021/ja208633g.

[71] S. Sathasivam, D.S. Bhachu, Y. Lu, N. Chadwick, S.A. Althabaiti, A.O. Alyoubi, S.N. Basahel, C.J. Carmalt, I.P. Parkin, Tungsten doped TiO 2 with enhanced photocatalytic

and optoelectrical properties via aerosol assisted chemical vapor deposition, Sci. Rep. 5 (2015) 1–10. doi:10.1038/srep10952.

[72] P.G. Gassman, D.W. Macomber, S.M. Willging, Isolation and Characterization of Reactive Intermediates and Active Catalysts in Homogeneous Catalysis, J. Am. Chem. Soc. 107 (1985) 2380–2388. doi:10.1021/ja00294a031.

[73] M. Seifollahi Bazarjani, M. Hojamberdiev, K. Morita, G. Zhu, G. Cherkashinin, C. Fasel, T. Herrmann, H. Breitzke, A. Gurlo, R. Riedel, Visible Light Photocatalysis with c-WO 3– x /WO 3 ×H 2 O Nanoheterostructures In Situ Formed in Mesoporous Polycarbosilane-Siloxane Polymer, J. Am. Chem. Soc. 135 (2013) 4467–4475. doi:10.1021/ja3126678.

[74] N. Huo, S. Yang, Z. Wei, J. Li, Synthesis of WO3 nanostructures and their ultraviolet photoresponse property, J. Mater. Chem C. 1 (2020) 3777. doi:10.1039/C3TC30527A.

[75] S. Eibl, B.C. Gates, H. Knözinger, Structure of WOx/TiO2 catalysts prepared from hydrous titanium oxide hydroxide: Influence of preparation parameters, Langmuir. 17 (2001) 107–115. doi:10.1021/la000977h.

[76] W. Smith, Z.-Y. Zhang, Y.-P. Zhao, Structural and optical characterization of WO[sub 3] nanorods/films prepared by oblique angle deposition, J. Vac. Sci. Technol. B Microelectron. Nanom. Struct. 25 (2007) 1875. doi:10.1116/1.2799968.

[77] R. Sivakumar, R. Gopalakrishnan, M. Jayachandran, C. Sanjeeviraja, Preparation and characterization of electron beam evaporated WO3 thin films, Opt. Mater. (Amst). 29 (2007) 679–687. doi:10.1016/j.optmat.2005.11.017.

[78] S. Rahimnejad, J.H. He, W. Chen, K. Wu, G.Q. Xu, Tuning the electronic and structural properties of WO3 nanocrystals by varying transition metal tungstate precursors, RSC Adv. 4 (2014) 62423–62429. doi:10.1039/c4ra10650d.

[79] Y. Li, Z. Wang, L. Sun, Z. Wang, S. Wang, X. Liu, Y. Wang, Investigation of oxygen vacancy and photoluminescence in calcium tungstate nanophosphors with different particle sizes, Mater. Res. Bull. 50 (2014) 36–41. doi:10.1016/j.materresbull.2013.10.022.

[80] E. Oakton, G. Siddiqi, A. Fedorov, C. Copéret, Tungsten oxide by non-hydrolytic sol-gel: Effect of molecular precursor on morphology, phase and photocatalytic performance, New J. Chem. 40 (2016) 217–222. doi:10.1039/c5nj01973g.

[81] V. Figueiredo, E. Elangovan, G. Gon??alves, P. Barquinha, L. Pereira, N. Franco, E. Alves, R. Martins, E. Fortunato, Effect of post-annealing on the properties of copper oxide thin films obtained from the oxidation of evaporated metallic copper, Appl. Surf. Sci. 254 (2008) 3949–3954. doi:10.1016/j.apsusc.2007.12.019.

[82] G. Leftheriotis, S. Papaefthimiou, P. Yianoulis, A. Siokou, Effect of the tungsten oxidation

states in the thermal coloration and bleaching of amorphous WO3 films, Thin Solid Films. 384 (2001) 298–306. doi:10.1016/S0040-6090(00)01828-9.

[83] G. Kovács, L. Baia, A. Vulpoi, T. Radu, É. Karácsonyi, A. Dombi, K. Hernádi, V. Danciu, S. Simon, Z. Pap, Applied Catalysis B : Environmental TiO_2 / WO_3 / Au nanoarchitectures ' photocat1. Kovács G, Baia L, Vulpoi A, et al (2014) Applied Catalysis B : Environmental TiO_2 / WO_3 / Au nanoarchitectures ' photocatalytic activity , "from degradation intermediates t, "Applied Catal. B, Environ. 147 (2014) 508–517. doi:10.1016/j.apcatb.2013.09.019.

[84] K. Vanheusden, W.L. Warren, C.H. Seager, D.R. Tallant, J.A. Voigt, B.E. Gnade, Mechanisms behind green photoluminescence in ZnO phosphor powders, J. Appl. Phys. 79 (1996) 7983–7990. doi:10.1063/1.362349.

[85] W.L. Kwong, N. Savvides, C.C. Sorrell, Electrodeposited nanostructured WO 3 thin films for photoelectrochemical applications, Electrochim. Acta. 75 (2012) 371–380. doi:10.1016/j.electacta.2012.05.019.

[86] G. Li Puma, V. Puddu, H.K. Tsang, A. Gora, B. Toepfer, Photocatalytic oxidation of multicomponent mixtures of estrogens (estrone (E1), 17β-estradiol (E2), 17α-ethynylestradiol (EE2) and estriol (E3)) under UVA and UVC radiation: Photon absorption, quantum yields and rate constants independent of photon absorp, Appl. Catal. B Environ. 99 (2010) 388–397. doi:10.1016/j.apcatb.2010.05.015.

[87] D.A. Armstrong, R.E. Huie, W.H. Koppenol, S. V. Lymar, G. Merenyi, P. Neta, B. Ruscic, D.M. Stanbury, S. Steenken, P. Wardman, Standard electrode potentials involving radicals in aqueous solution: Inorganic radicals (IUPAC Technical Report), Pure Appl. Chem. 87 (2015) 1139–1150. doi:10.1515/pac-2014-0502.

[88] Y. Tae Kwon, K. Yong Song, W. In Lee, G. Jin Choi, Y. Rag Do, Photocatalytic behavior of WO3-loaded TiO2 in an oxidation reaction, J. Catal. 191 (2000) 192–199. doi:10.1006/jcat.1999.2776.

[89] J. Knöppel, S. Zhang, F.D. Speck, K.J.J. Mayrhofer, C. Scheu, S. Cherevko, Time-resolved analysis of dissolution phenomena in photoelectrochemistry – A case study of WO3 photocorrosion, Electrochem. Commun. 96 (2018) 53–56. doi:10.1016/j.elecom.2018.09.008.

[90] J. Knöppel, A. Kormányos, B. Mayerhöfer, A. Hofer, M. Bierling, J. Bachmann, S. Thiele, S. Cherevko, Photocorrosion of WO 3 Photoanodes in Different Electrolytes , ACS Phys. Chem. Au. 1 (2021) 6–13. doi:10.1021/acsphyschemau.1c00004.

[91] Z. Frontistis, V.M. Daskalaki, A. Katsaounis, I. Poulios, D. Mantzavinos, Electrochemical

enhancement of solar photocatalysis: Degradation of endocrine disruptor bisphenol-A on Ti/TiO2 films, Water Res. 45 (2011) 2996–3004. doi:10.1016/j.watres.2011.03.030.

[92] M. V. De Liz, R.M. De Lima, B. Do Amaral, B.A. Marinho, J.T. Schneider, N. Nagata, P. Peralta-Zamora, Suspended and immobilized TiO2 photocatalytic degradation of estrogens: Potential for application in wastewater treatment processes, J. Braz. Chem. Soc. 29 (2018) 380–389. doi:10.21577/0103-5053.20170151.

[93] W. Zhang, Y. Li, Y. Su, K. Mao, Q. Wang, Effect of water composition on TiO 2 photocatalytic removal of endocrine disrupting compounds (EDCs) and estrogenic activity from secondary effluent, J. Hazard. Mater. 215–216 (2012) 252–258. doi:10.1016/j.jhazmat.2012.02.060.

[94] K. Sornalingam, A. McDonagh, J.L. Zhou, M.A.H. Johir, M.B. Ahmed, Photocatalysis of estrone in water and wastewater: Comparison between Au-TiO_2 nanocomposite and TiO_2, and degradation by-products, Sci. Total Environ. 610–611 (2018) 521–530. doi:10.1016/j.scitotenv.2017.08.097.

[95] R.R. Chowdhury, P.A. Charpentier, M.B. Ray, Photodegradation of 17β-estradiol in aquatic solution under solar irradiation: Kinetics and influencing water parameters, J. Photochem. Photobiol. A Chem. 219 (2011) 67–75. doi:10.1016/j.jphotochem.2011.01.019.

[96] J. Yano, T. Morita, K. Shimano, Y. Nagami, S. Yamasaki, Selective ethylene formation by pulse-mode electrochemical reduction of carbon dioxide using copper and copper-oxide electrodes, J. Solid State Electrochem. 11 (2007) 554–557. doi:10.1007/s10008-006-0181-4.

[97] N.C. Verissimo, A. Cremasco, C.A. Rodrigues, R. Bertazzoli, R. Caram, In situ characterization of the effects of Nb and Sn on the anatase-rutile transition in TiO 2 nanotubes using high-temperature X-ray diffraction, Appl. Surf. Sci. 307 (2014) 372–381. doi:10.1016/j.apsusc.2014.04.040.

Table 1. Chemical composition (wt.%) and quantify of phases composition of the substrates

Electrode	Elemental			Substrate Phases – Rietveld Method			
	Ti(wt%)	W(wt%)	Error (%)	Ti-α / Ti-α doped (wt%)	Ti-β (wt%)	W precipitate (wt%)	GoF**
Ti-0.5W	99.50*	0.50*	0.742	100.0	-	-	1.7
Ti-2.5W	97.73	2.27	0.786	96.740	2.992	0.266	1.9
Ti-5.0W	95.33	4.66	0.868	92.136	7.436	0.428	2.1

(*) Analysis confirmed by ICP-MS; (**) goodness-of-fit.

Table 2. XPS analysis: relative peak area to molar percentages (MP) of Ti^{3+} and Ti^{4+} species from Ti 3p region and W^{+4}, W^{+5} and W^{+6} species from W 4f spectra of the NT/Ti-0.5W, NT/Ti-2.5W and NT/Ti-5.0W samples.

Sample	**MP (%) Ti 3p**		**MP (%) W 4f**		
	Ti^{+4}	**T^{+3}**	**W^{+4}**	**W^{+5}**	**W^{+6}**
Ti-0.5W	63.02	5.22	0.43	31.33	-
Ti-2.5W	43.17	0.30	2.94	45.33	8.25
Ti-5.0W	23.54	1.45	1.14	33.06	40.81

Table 3. Dependence of the photocurrent for the NT/Ti-xW photoelectrodes on the bias voltage and UV-Vis and visible light irradiation from cyclic sweep voltammetry (Fig 7 b) at 1.3 V *vs.* Ag/AgCl.

Electrode	**UV irradiation (i / mA.cm^{-2})**	**Visible Light irradiation (i / mA.cm^{-2})**
NT/TiO$_2$	1.39	0.22
NT/Ti-0.5W	1.64	0.34
NT/Ti-2.5W	1.78	0.75
NT/Ti-5.0W	2.34	1.01

Table 4. Kinect parameters of the photocatalytic degradation of E1 and EE2 from matrix natural water under UV-vis irradiation.

Estrogen	Electrode	Reaction constant ($k \times 10^{-2}$ min^{-1})	Time 1/2 (min)	R^2	χ^2
E1	NT/TiO_2	3.3	20.88	0.969	0.011
	NT/Ti-0.5W	4.1	16.93	0.996	0.009
	NT/Ti-2.5W	4.5	15.40	0.997	0.007
	NT/Ti-5.0W	9.9	6.98	0.993	0.071
EE2	NT/TiO_2	1.7	39.32	0.991	0.004
	NT/Ti-0.5W	2.0	33.55	0.992	0.002
	NT/Ti-2.5W	2.3	29.86	0.997	0.001
	NT/Ti-5.0W	2.5	0.999	27.11	0.003

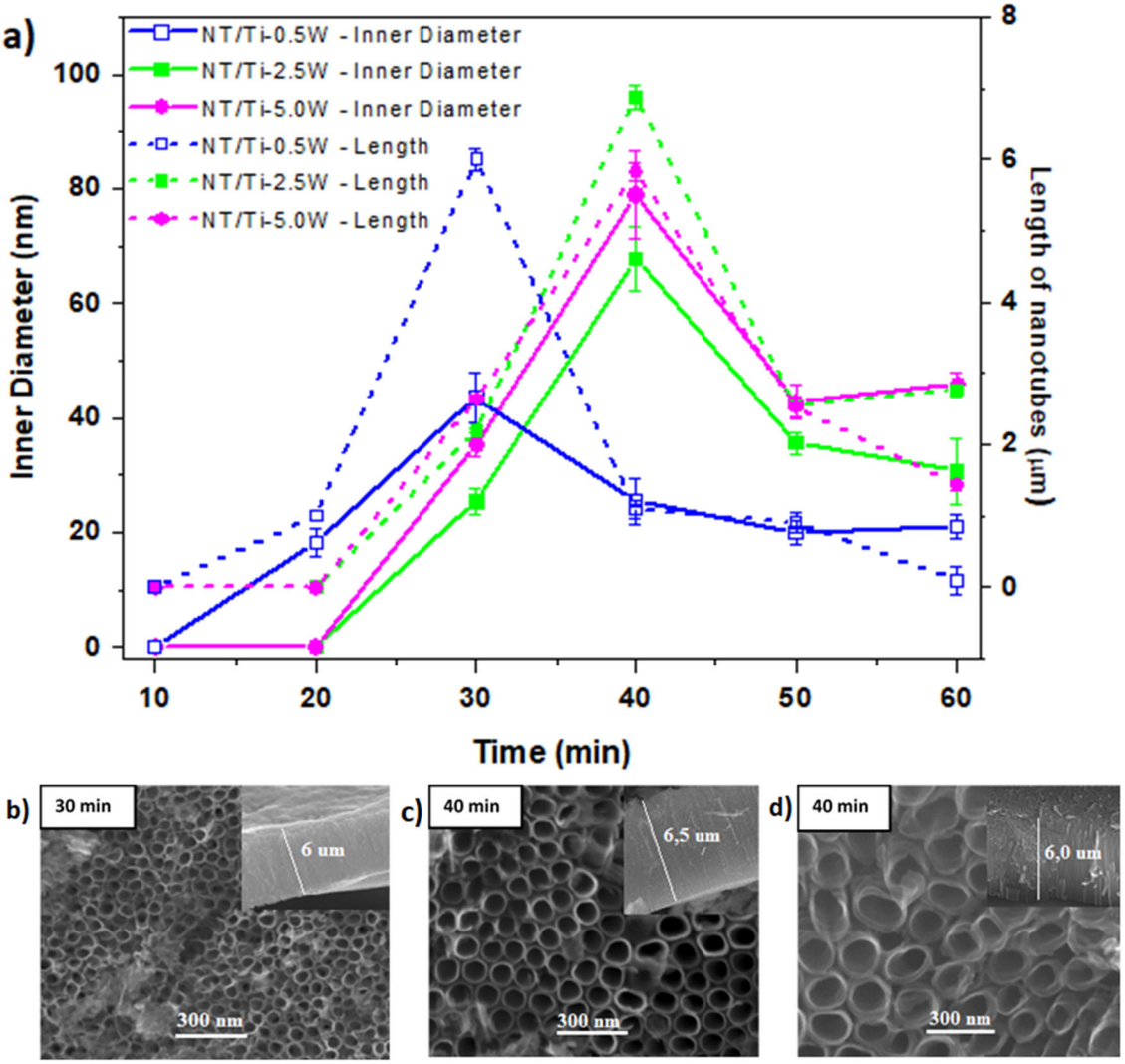

Figure 1. Influence of the anodization time at 120 V of Ti-x%wt.W alloys (a) inner diameter of nanotubes and electronic microscopy images as function of anodization time for: (b) NT/Ti-0.5W (c) NT/Ti-2.5W and (d) NT/Ti-5.0W.

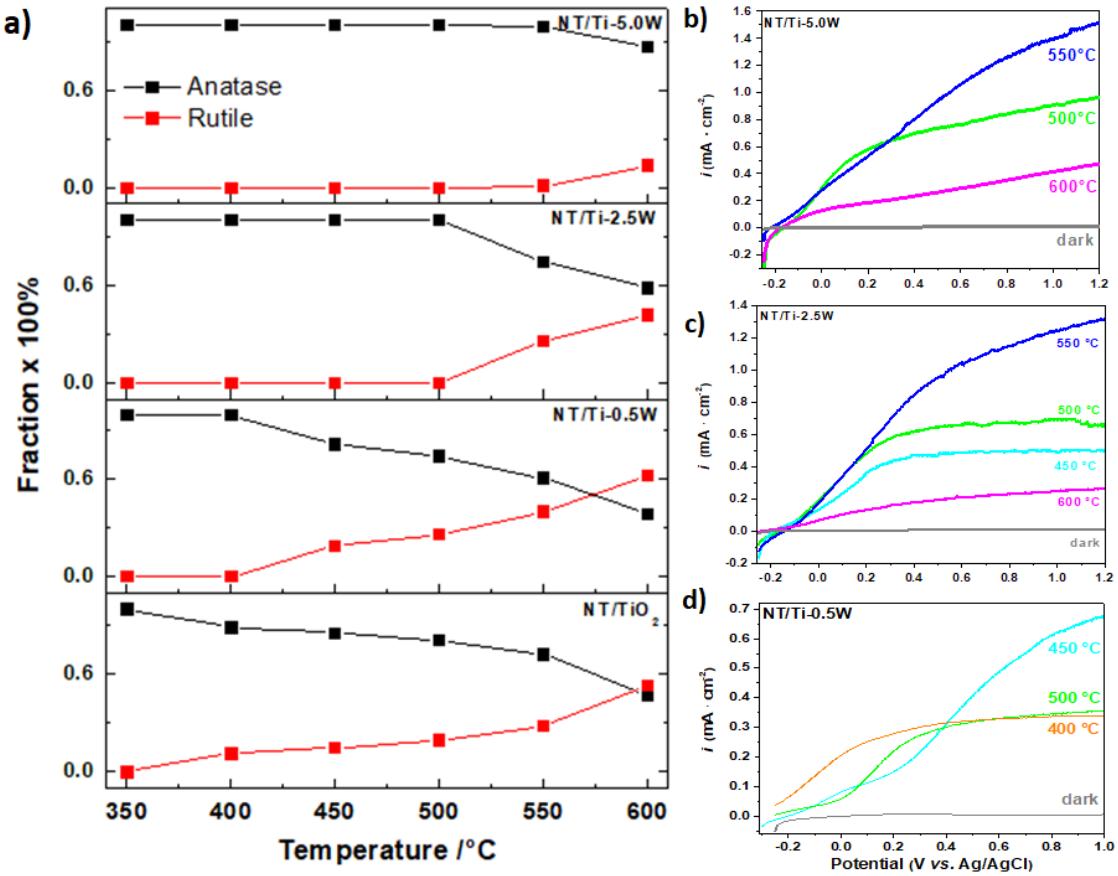

Figure 2. Relation of titanium crystalline phases anatase and rutile after heat treatment of layer grown under Ti pure and Ti-xwt.%W substrates to different temperatures (350 to 600 °C).

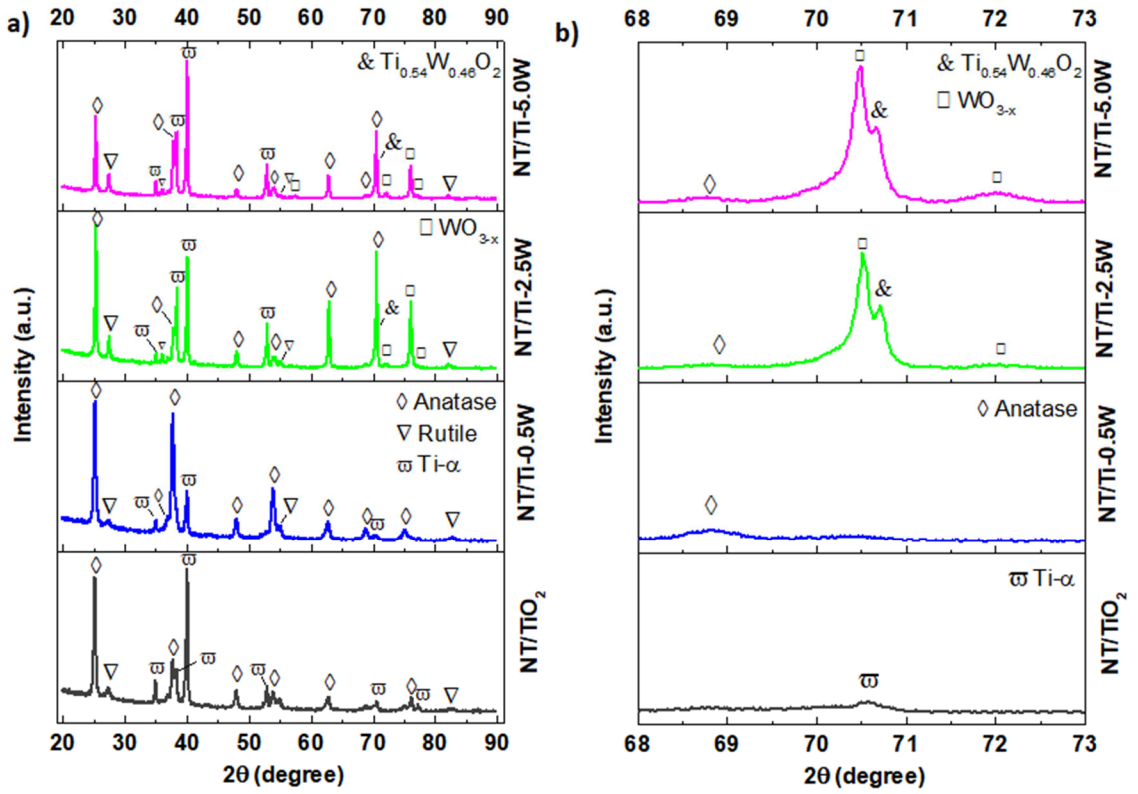

Figure 3. XRD patterns of the NT/TiO_2-450 °C, NT/Ti-0.5W-450 °C, NT/Ti-2.5W-550 °C and NT/Ti-5.0W-550 °C. (b) Details of XRD measurements for 2θ = 68 – 73°.

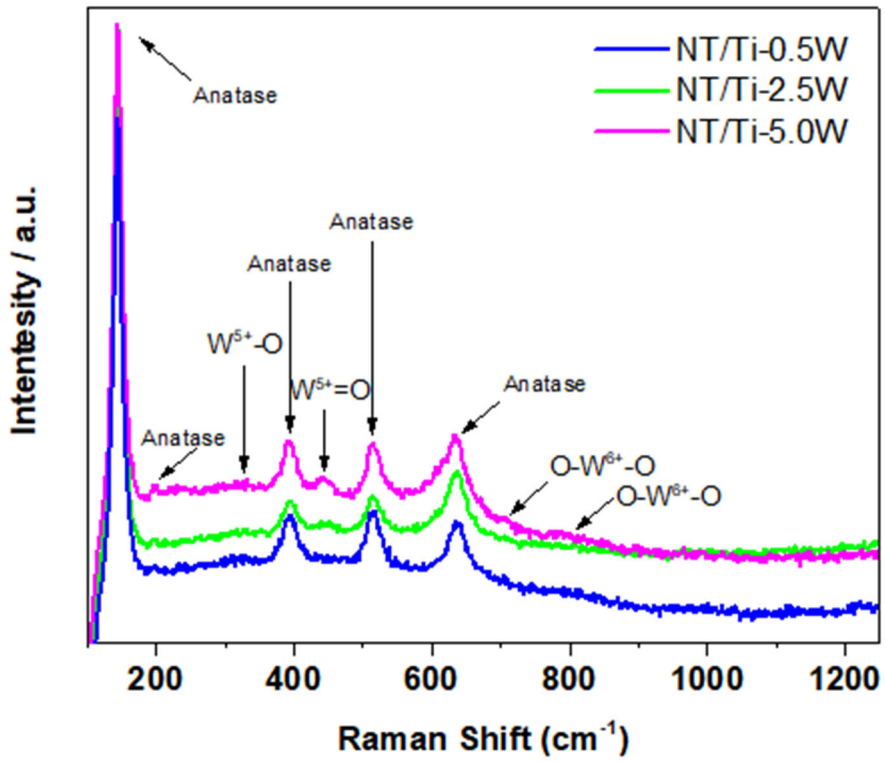

Figure 4. Raman spectrum of NT/Ti-0.5W (blue), NT/Ti-2.5W (green) and NT/Ti-5.0W (pink).

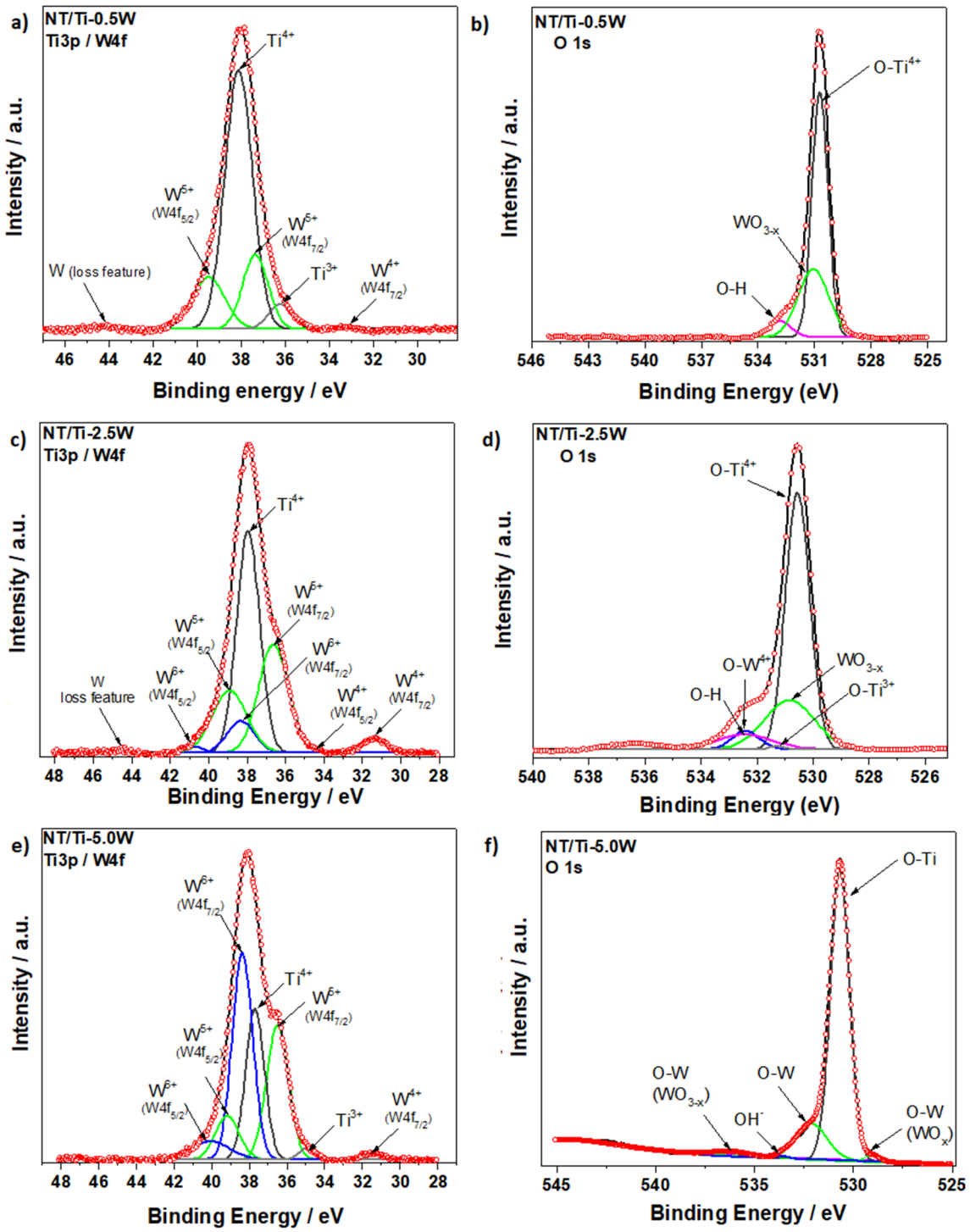

Figure 5. In order to identify the composition and the concentration of W species in oxide layer, XPS and Rietveld analysis were carried out. (a) NT/Ti-0.5W (b) NT/Ti-2.5W (c) NT/Ti-5.0W

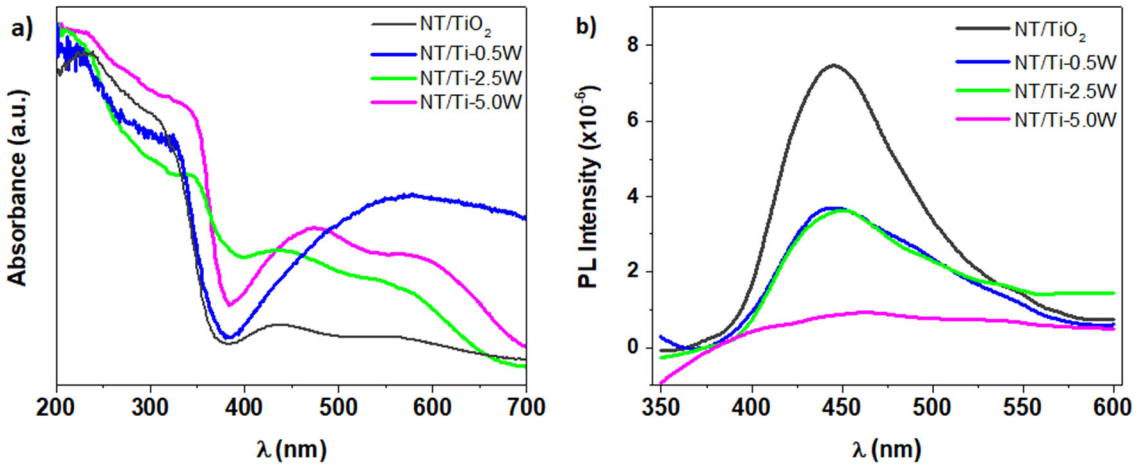

Figure 6. (a) UV–Vis diffused reflectance spectra and (b) photoluminescence spectra (PL) of the NT/TiO_2, NT/Ti-0.5W, NT/Ti-2.5W and NT/Ti-5.0W.

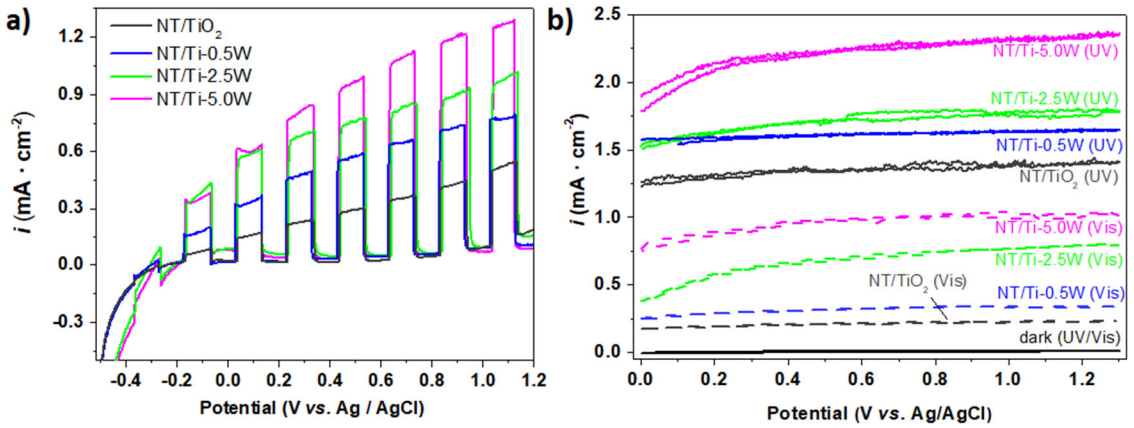

Figure 7. Photovoltammogram of the NT/TiO_2, NT/Ti-0.5W, NT/Ti-2.5W and NT/Ti-5.0W electrodes (a) linear sweep voltammetry scans were performed under interrupted UV–Visirradiation in 0.2 M Na_2SO_4 (pH 5.7) with a scan rate of 10 mV/s. (b) Cyclic photocurrent under UV–Vis (solid line) and visible light (dash line) in 0.5 M HCOONa.

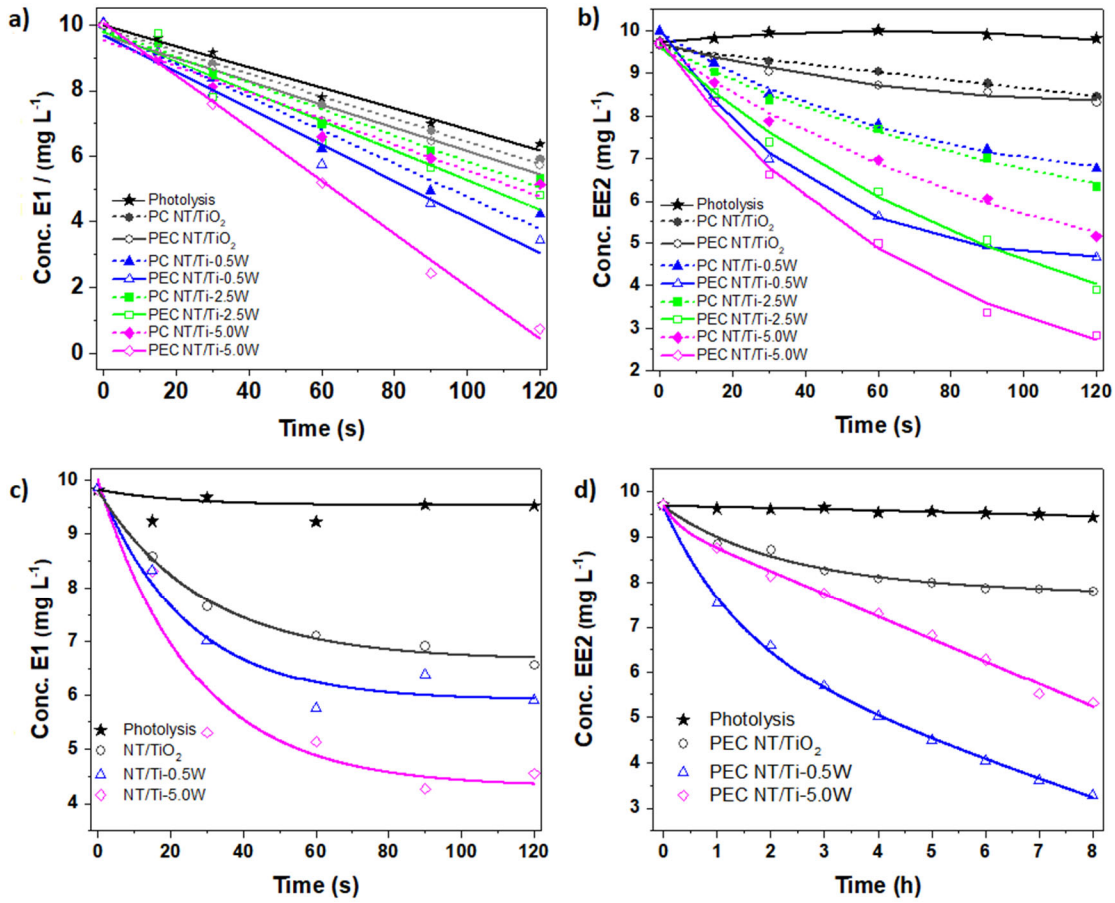

Figure 8. Degradation under UV-Vis irradiation during 120 s for: (a) E1 and (b) EE2. Photoelectrocatalytic under visible light irradiation for: (c) E1 during 120 s and (d) EE2 during 8 hours. Initial condition: solution of 10 mg L^{-1} E1 (pH 6) or EE2 (pH 4) diluted in distilled water.

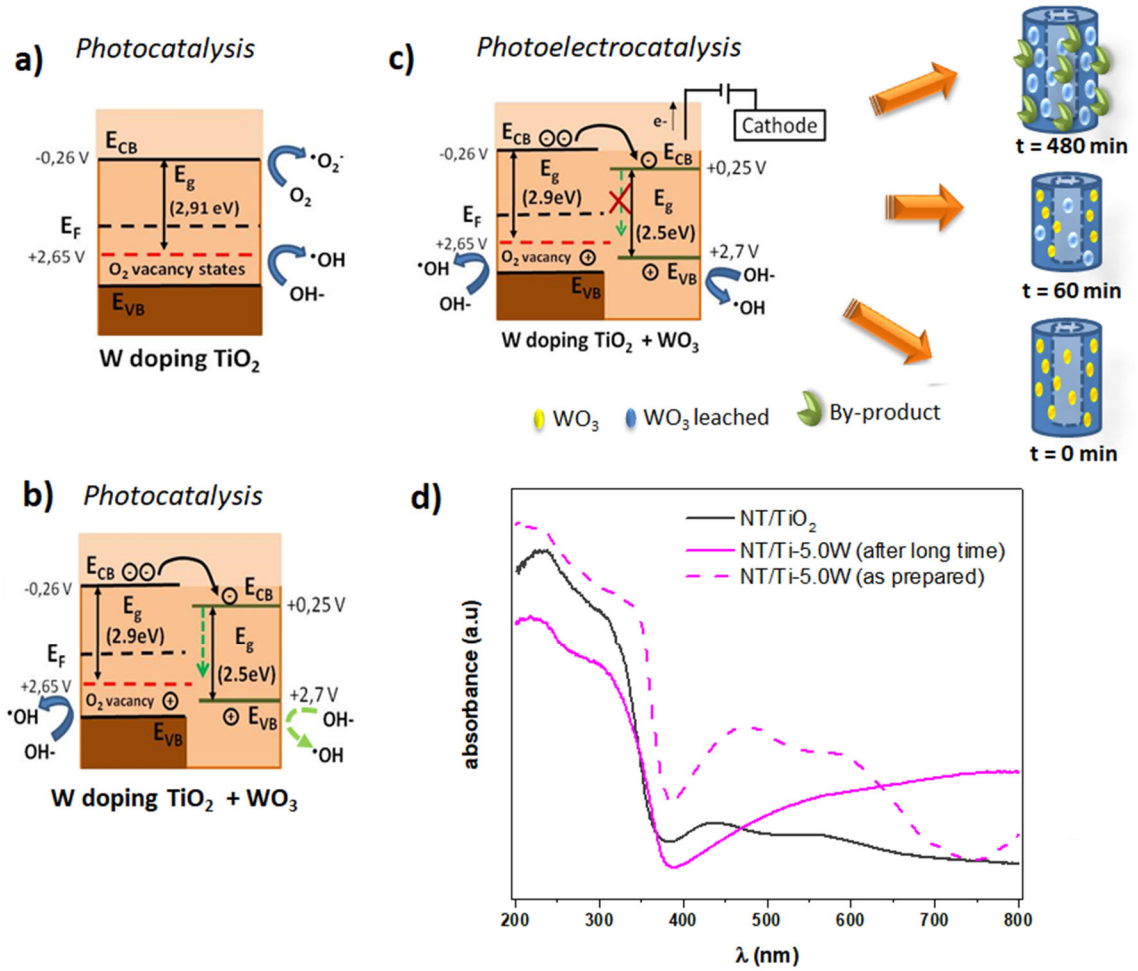

Figure 9. Schematic representation of the charge-transfer mechanism on NT/Ti-xW for degradation estrones under UV-vis and visible light. (a) dopped electrode of NT/Ti-0.5W (b) Photocatalytic process using NT-Ti-5.0W (c) Photoelectrocatalytic process using NT-Ti-5.0W (d) DRS spectra of NT/Ti-5.0W measured as prepared electrode and after photoelectrocatalytic process of estrones in prolonged and short period of time under UV-Vis and / or visible irradiation.

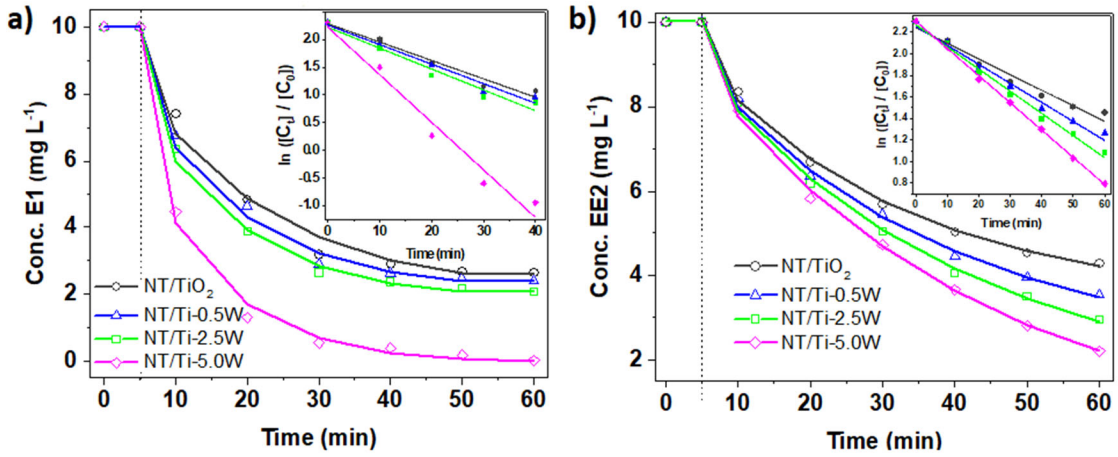

Figure 10. Photoelectrocatalytic degradation of (a) E1 and (b) EE2 in a real matrix water under UV-Vis irradiation. Inset: Kinetic profile of absorption spectra adjusted for pseudo-first order of hormones removal.

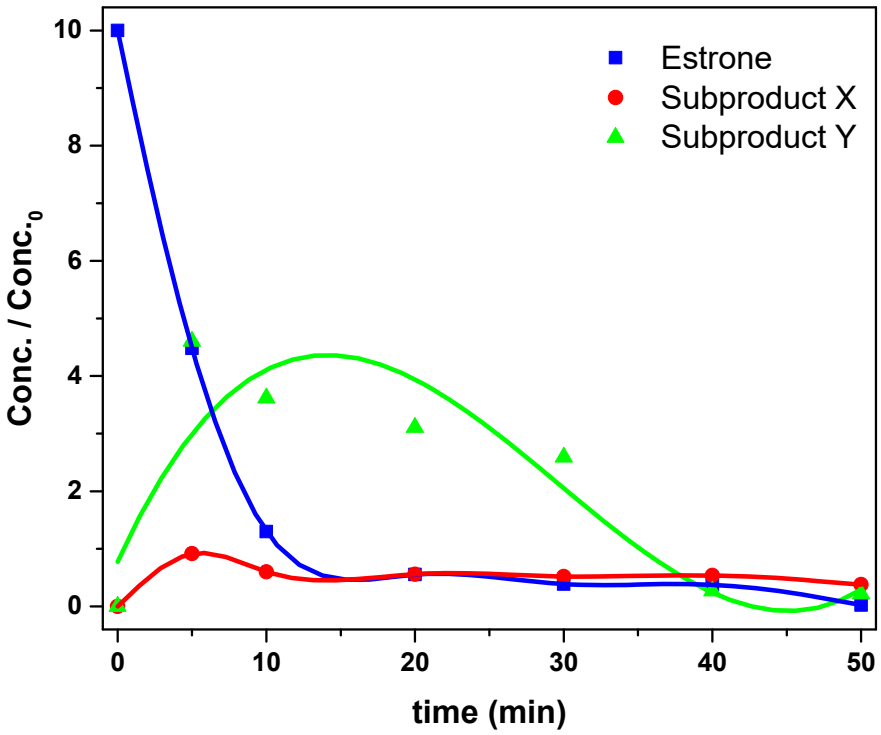

Figure 11. Concentration evolution of estrone in real water matrix and its derivatives. Process of NT/Ti-5.0W photoelectrocatalysis at pH 6 and under UV-Vis irradiation.

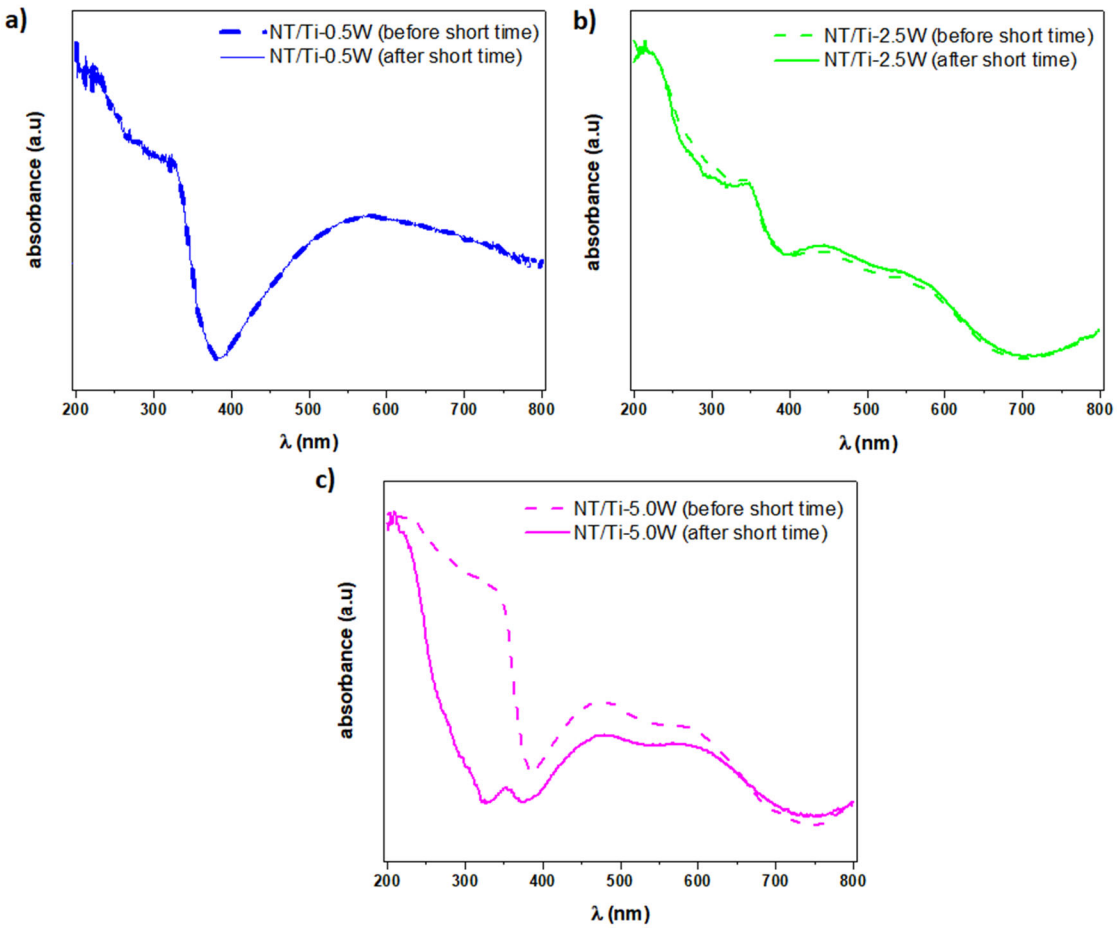

Figure 12. Comparing the DRS spectra of NT/Ti-xW measured before and after photoelectrocatalytic process of estrones in short period of time under UV-Vis irradiation: (a) NT/Ti-0.5W (b) NT/Ti-2.5W (c) NT/Ti-5.0W.